

EPA-650/4-74-044

NOVEMBER 1974

Environmental Monitoring Series

**LABORATORY
AND NUMERICAL SIMULATION
OF PLUME DISPERSION
IN STABLY STRATIFIED FLOW
OVER COMPLEX TERRAIN**



Office of Research and Development
U.S. Environmental Protection Agency
Washington, DC 20460

LABORATORY AND NUMERICAL SIMULATION OF PLUME DISPERSION IN STABLY STRATIFIED FLOW OVER COMPLEX TERRAIN

by

Jung-Tai Lin, Hsien-Ta Liu, Yih-Ho Pao,
Douglas K. Lilly, Moshi Israeli, and Steven A. Orszag

Flow Research, Inc.
1819 S. Central Avenue
Suite 72
Kent, Washington 98031

Contract No. 68-02-0800
ROAP No. 21ADO
Program Element No. 1A1009

EPA Project Officer: William H. Snyder

Meteorology Laboratory
National Environmental Research Center
Research Triangle Park, North Carolina 27711

Prepared for

OFFICE OF RESEARCH AND DEVELOPMENT
U.S. ENVIRONMENTAL PROTECTION AGENCY
WASHINGTON, D.C. 20460

November 1974

EPA REVIEW NOTICE

This report has been reviewed by the National Environmental Research Center - Research Triangle Park, Office of Research and Development, EPA, and approved for publication. Approval does not signify that the contents necessarily reflect the views and policies of the Environmental Protection Agency, nor does mention of trade names or commercial products constitute endorsement or recommendation for use.

This document is available to the public for sale through the National Technical Information Service, Springfield, Virginia 22161.

LABORATORY AND NUMERICAL SIMULATION OF
PLUME DISPERSION IN STABLY STRATIFIED FLOWS
OVER COMPLEX TERRAIN

by

Flow Research, Inc., Kent, Washington 98031

Forward

Flow Research was under contract with the Environmental Protection Agency (Contract No. 68-02-0800) to investigate plume dispersion in stably stratified flows over complex terrain. Two tasks are involved:

Task I - Laboratory simulation of plume dispersion in stably stratified flow over a complex terrain, which is covered in Flow Research Report No. 29.

Task II - A feasibility study of numerical simulation of plume dispersion in stably stratified flows over complex terrain, which is covered in Flow Research Note No. 40 and Flow Research Report No. 30.

These three reports, each of which can be separated as an individual report, are bound together under the title Laboratory and Numerical Simulation of Plume Dispersion in Stably Stratified Flows over Complex Terrain. The order of the binding is task oriented.

TASK I

LABORATORY SIMULATION OF PLUME DISPERSION IN
STABLY STRATIFIED FLOWS OVER
A COMPLEX TERRAIN

BY

JUNG-TAI LIN

HSIEN-TA LIU

YIH-HO PAO

Laboratory Simulation of Plume Dispersion in Stably
Stratified Flows over a Complex Terrain

by

Jung-Tai Lin, Hsien-Ta Liu, and Yih-Ho Pao
Flow Research, Inc., Kent, Washington 98031

Abstract

Laboratory simulations were conducted in a stably stratified towing tank to investigate the effects of stability and terrain on plume dispersion under extreme atmospheric conditions. A three dimensional model was towed through the tank to simulate flow over complex terrain. The terrain model contained the essential features of a complex terrain, namely, mountains, mountain ridges and valleys. A stack was located in the valley upstream of the mountain ridge between two mountain peaks. The simulation scaling factor was 1:2500. The stack Froude number was 3; the stack Reynolds number was 530; and the internal Froude number F_h based on the mountain ridge height ranged from 1 to 3.

The characteristics of plume dispersion were investigated using shadowgraph and dye visualization. With reference to plume dispersion over a flat plate, the terrain effects revealed from visualization results are:

- 1) The plume rise and spread increase as a result of the reduction of the local flow speed-- the upstream blocking phenomenon;
- 2) The lateral spread near the upstream side of the ridge is enhanced significantly by the lateral flow around the terrain model;
- 3) Accumulation of pollutants occurs in a semi-stagnant region just upstream and below the ridge;
- 4) Downstream of the ridge, pollutants carried around and over the terrain model remain aloft for small F_h , but are carried downward along the lee surface as F_h increases.

The turbulent velocity and density in the plume were measured with hot-film and conductivity probes. The normalized turbulent intensities and flatness factors of velocity and density fluctuations are approximately self-similar.

The mean and root-mean-square pollutant concentrations, using temperature as a tracer, were measured on the upstream slope of the terrain model. Highest concentrations occur at stations on the ridge.

Table of Contents

	<u>Page</u>
Abstract	i
Table of Contents	iii
Nomenclature	iv
1. Introduction	1
2. Principles of Laboratory Simulation	3
3. Experimental Facilities and Methods	6
3.1 The Stratified Towing Tank	6
3.2 The Terrain Model and Platform	6
3.3 The Effluent Injection Device	7
3.4 Flow Visualization Techniques	8
3.5 Hot-Film Anemometer, Conductivity Gauge, and Temperature Gauge	8
4. Flow Visualizations	10
4.1 Plume Dispersion in Stratified and Nonstratified Flows over a Flat Plate	10
4.2 Plume Dispersion in a Stratified Flow over the Terrain Model	12
5. Velocity, Density and Pollutant Concentration Measurements	15
6. Conclusions	17
7. References	19
Table 1	21
Table 2	22
Figures	23

NOMENCLATURE

Dimensions of each term are given in parenthesis: ℓ = length, t = time,
 τ = temperature, m = mass.

$a_i, i = 0, \dots, 5$ = Coefficients defined in Eq. (3.1)

D = Stack Diameter (ℓ)

F = Buoyancy Flux of Plume ($\ell^4 t^{-3}$), $g \frac{\Delta \rho}{\rho_a} \frac{D^2 W_s}{4}$

F_D = Stack Froude number (Dimensionless), $\frac{W_s}{\sqrt{\frac{\Delta \rho}{\rho_s} g D}}$

F_H = Internal Froude number based on the stack height (Dimensionless)
 $= \frac{U_\infty}{NH}$

F_h = Internal Froude number based on the ridge height (Dimensionless)
 $= \frac{U_\infty}{\frac{1}{2\pi} \sqrt{\frac{g}{\rho_a} \frac{d\bar{\rho}}{dz} h}} = \frac{U_\infty}{Nh}$

g = Gravitational Acceleration (ℓt^{-2})

$h(x,y)$ = Terrain height (ℓ)

h_o = Mountain peak height (ℓ)

H = Stack height (ℓ)

K = Ratio of effluent velocity to free stream velocity (Dimensionless)
 $= \frac{W_s}{U_\infty}$

N = Brunt-Vaisala frequency (cycle t^{-1}), $\frac{1}{2\pi} \sqrt{\frac{g}{\rho_a} \frac{d\bar{\rho}}{dz}}$

R_D = Stack Reynolds number (Dimensionless), $\frac{W_s D}{\nu}$

R_h = Reynolds number based on the ridge height (Dimensionless)
 $= \frac{U_\infty h}{\nu}$

s = Stability parameter (cycle² t^{-2}), $(2\pi N)^2$

t = Time (t)

U = Instantaneous velocity component in x direction (ℓt^{-1})

- \bar{U} = Mean velocity component in x direction (ℓt^{-1})
 U_a = Mean velocity component in x direction at $z = H$ (ℓt^{-1})
 U_∞ = Free stream velocity (ℓt^{-1})
 u = Fluctuating velocity component in x direction, (ℓt^{-1})
 W_s = Stack effluent velocity (ℓt^{-1})
 x, y, z = Cartesian coordinate axes in longitudinal, lateral, and vertical directions, respectively (ℓ)
 x_o, y_o = x and y coordinates of the saddle point on the mountain ridge (ℓ)
 Z = Plume rise determined from visualization results (based on the stack exit level) (ℓ)
 Z_u, Z_σ = Plume rise defined as the plume trajectories at which $\sqrt{u^2} = \sqrt{u_{\max}^2}$ and $\sqrt{\sigma^2} = \sqrt{\sigma_{\max}^2}$, respectively (ℓ)
 α = Longitudinal entrainment coefficient (Dimensionless)
 β = Cross-flow entrainment coefficient (Dimensionless)
 $\Delta Y, \Delta Z$ = Lateral and vertical spreads of plume determined from visualization results (ℓ)
 $\Delta Z_u, \Delta Z_\sigma$ = Vertical spreads defined as the width between the plume boundaries at which $\sqrt{u^2} = \sqrt{u_{\max}^2}/2$ and $\sqrt{\sigma^2} = \sqrt{\sigma_{\max}^2}/2$, respectively.
 Γ = Adiabatic lapse rate ($\tau \ell^{-1}$)
 τ = Lapse Rate ($\tau \ell^{-1}$)
 h = Mountain ridge height (ℓ)
 ρ = Density ($m \ell^{-3}$)
 $\bar{\rho}$ = Mean density of the ambient fluid ($m \ell^{-3}$)
 ρ_a = Density of ambient fluid at stack exit level ($m \ell^{-3}$)
 ρ_s = Stack effluent density ($m \ell^{-3}$)
 $\Delta \rho = \rho_s - \rho_a$ ($m \ell^{-3}$)
 ν = Kinematic viscosity ($\ell^2 t^{-1}$)
 Σ = Reduced density ($m \ell^{-3}$), $(\rho - 1) \times 1000$
 Σ_s = Reduced density of the effluent ($m \ell^{-3}$), $(\rho_s - 1) \times 1000$

σ = Fluctuating reduced density ($m\ell^{-3}$)

θ = Temperature (τ)

θ_a = Temperature of ambient fluid at stack exit level (τ)

θ_s = Effluent temperature (τ)

θ = Fluctuating temperature (τ)

Laboratory Simulation of Plume Dispersion in Stably
Stratified Flows over a Complex Terrain

by

Jung-Tai Lin, Hsien-Ta Liu, and Yih-Ho Pao

Flow Research, Inc., Kent, Wash. 98031

1. Introduction

Serious air-pollution episodes usually occur in the areas where the terrain features are dominantly irregular and complex, and during the periods when the atmosphere is stably stratified. In a stably stratified flow over a complex terrain, individual flow phenomena, namely, blocking, velocity concentration, flow separation, lee waves, drainage, and heated-island effects, influence the transport of pollutants in their own particular ways. Therefore, the combined effects of the flow phenomena on air-pollution problems are expectedly complicated. The present study attempts to understand through laboratory experiments terrain effects, not including drainage and heated-island effects, on the pollutant transport in stably stratified flows.

For simulating the plume dispersion in a neutral atmosphere over a complex terrain, Hino (1968) conducted experiments in a wind tunnel. Veenhuizen et al. (1973) conducted similar experiments in a towing tank. Orgill et al. (1970) simulated the dispersion of pollutants in stably stratified flows over a complex terrain in a wind tunnel by cooling with dry ice the flow near the terrain surface. In the present investigation, the dispersion of a bent-over plume in stably stratified flows (with linear density profiles in a towing tank) over an idealized three-dimensional terrain model were studied. Both flow visualizations and probe measurements were conducted in an attempt to gain further insight into the problem.

In this report, the principles of laboratory simulation are investigated in Section 2 to determine the basic simulation parameters for the plume dispersion in a stably stratified flow over a complex terrain. The experimental facilities are described in Section 3. Flow visualization results of plume dispersion over a flat plate and over a 3-D terrain are

presented in Section 4; the experiments with the flat plate were conducted to provide a reference for investigating the terrain effects. The results of velocity and density measurements in the plume and pollutant concentration measurements on the terrain surface are presented in Section 5. Conclusions are given in Section 6.- In addition, flow visualizations are presented in Flow Research Movie No. 6 as a part of the report.

2. Principles of Laboratory Simulation

Geometric, kinematic, and dynamic similarities must be satisfied in the simulation of plume dispersion in a stratified flow over a complex terrain. The equation for plume rise in a stably stratified atmosphere, and the equation for the wind field are, respectively

$$Z = f(x, y, D, H, h(x, y), W_s, \theta_s, \theta_a, U_\infty, U, \gamma - \Gamma, g, \nu) \quad (2.1)$$

and

$$U = g(x, y, z, D, H, h(x, y), \gamma - \Gamma, U_\infty, g, \nu) \quad (2.2)$$

where Z is the plume trajectory (the centroid of the plume cross-section) above the stack, x, y are the respective longitudinal and lateral coordinates referenced to the stack base, D is the stack diameter, H is the stack height, $h(x, y)$ is the terrain profile, W_s is the effluent speed, θ_s is the temperature of the effluent, θ_a is the ambient fluid temperature, U is the free stream wind speed, γ is the lapse rate of atmosphere, Γ is the adiabatic lapse rate, g is the gravitational acceleration, and ν is the kinematic viscosity of the air. Figure 1 shows a definition sketch of the most relevant variables.

Based on dimensional arguments, the following nondimensional equations can be derived from Eq. (2.1) and Eq. (2.2),

$$\text{and} \quad Z/D = f(x/D, y/D, H/D, h(x/D, y/D)/D, U/U_\infty, K, F_D, F_h, R_D) \quad (2.3)$$

$$U/U_\infty = g(x/D, y/D, z/D, H/D, h(x/D, y/D)/D, F_h, R_h), \quad (2.4)$$

where

$$K = \frac{W_s}{U_\infty} \quad \text{is the velocity ratio,}$$

$$F_D = \frac{W_s}{\sqrt{gD \frac{\theta_s - \theta_a}{\theta_a}}} \quad \text{is the stack Froude number,}$$

$$F_h = \frac{U_\infty}{\frac{1}{2\pi} \sqrt{\frac{g(\gamma - \Gamma)}{\theta_a}} h} \quad \text{is the internal Froude number,}$$

$$R_D = \frac{W_s D}{\nu} \quad \text{is the stack Reynolds number,}$$

$$R_h = \frac{U_\infty h}{\nu} \quad \text{is the terrain Reynolds number,}$$

and h is a characteristic height of the terrain.

Geometric similarity is satisfied when Z/D , H/D , and $h(x/D, y/D)/D$ in the laboratory have the same values as those in the field. When K and U/U_∞ in the laboratory are equal to those in the field, kinematic similarity is satisfied. Plume dispersion is dynamically simulated when F_D , F_h , R_D , and R_h in the laboratory are equal to those in the field.

In the laboratory simulation, the fulfillment of the dynamic similarity of F_D and F_h is usually not a problem. The dynamic similarity of the stack Reynolds number R_D cannot be fulfilled as the Reynolds number in the laboratory is usually about 3-4 orders of magnitude smaller. However, experience (Hoult et al. 1972) has shown that the Reynolds number effect is not important as long as the plume is turbulent in a nonstratified fluid. The Reynolds number effect on plume dispersion in the stably stratified fluid will be investigated in Section 4.1.

In the dimensional analysis expressed in Eqs. (2.3) and (2.4), the turbulent structure in the atmospheric boundary layer is not considered. In the case of a neutral atmosphere, the boundary layer may have a thickness of about 300m which is higher than the average stack height of about 150m, and thus, in the laboratory simulation of plume dispersion, turbulent characteristics in the atmospheric boundary layer must be simulated properly. In the case of a stably stratified atmosphere, the boundary layer is thin and the atmosphere is basically not turbulent (Slade, 1969). Hence, in the simulation of plume dispersion in a stably stratified flow, the boundary layer and the terrain Reynolds number need not be critically simulated as long as the stack height is greater than the boundary layer thickness and the plume dispersion occurs outside the boundary layer.

The laboratory simulation of plume dispersion was conducted in a stratified towing tank in which a wide range of K , F_D , and F_h can be achieved to meet the various field conditions. A salt solution was used for both the effluent and the ambient stratified fluid. The stack Froude number F_D and the internal Froude number F_h are then redefined as

$$F_D = \frac{W_s}{\sqrt{gD \frac{\Delta \rho}{\rho_s}}} , \quad (2.5)$$

and

$$F_h = \frac{U_\infty}{Nh} , \quad (2.6)$$

where $\Delta\rho = \rho_s - \rho_a$, ρ_s is the density of effluent at the stack exit, ρ_a is the density of the ambient fluid at the level of stack exit and N is the Brunt-Vaisala frequency (cycle/sec) defined as $N = \frac{1}{2\pi} \sqrt{-\frac{g}{\rho_a} \frac{d\rho}{dz}}$, where $\frac{d\rho}{dz}$ is the mean density gradient of the ambient fluid.

A modeling example is given in the following by considering a prototype stack of 127 m height and 7.94 m in diameter. The effluent temperature θ_s is 160°C ; the effluent velocity W_s is 20.4 m/sec; and the ambient temperature at the level of the stack exit θ_a is 5°C . The stack Froude number is therefore $F_D = 3.09$. Further consider a stable atmosphere having a lapse rate $\gamma = .025^\circ\text{C/m}$, a wind speed $U_\infty = 6$ m/sec, and a characteristic height of the terrain $h = 407$ m. The internal Froude number is therefore $F_h = 2.64$; and the velocity ratio is $K = 3.4$. If a scaling factor 1:2500 is selected for the laboratory simulation, the model stack height and diameter will be 5.0 cm and 0.32 cm, respectively; and the characteristic height of the model terrain is 16.3 cm. To satisfy the simulation of the internal Froude number F_h , $U_\infty = 6$ cm/sec and $N = .14$ cycle/sec are used. To meet the requirements of the velocity ratio K and the stack Froude number F_D , $W_s = 20.4$ cm/sec, $\rho_s = 1.175$ gm/cm³, and $\rho_a = 1.015$ gm/cm³ are used.

3. Experimental Facilities and Methods

3.1 The Stratified Towing Tank

The plume dispersion experiments were performed in a stratified towing tank, 18.3m long, 1.2m wide, and .91m deep. See Flow Research Report No. 4 (Pao et al. 1971) for a detailed description of the stratified towing tank. In the following, some special features of the tank are described briefly.

The towing tank was designed and constructed for investigating turbulent wake and internal wave phenomena in stably stratified fluids.

- 1) It has transparent side, bottom, and end walls to allow flow visualization from all directions.
- 2) It has a filling system to provide a stratified fluid at a predetermined stratification within four hours. Salt (NaCl) solution is the working fluid for making a stratified fluid. The temperature of the fluid is controlled within 0.1°C .
- 3) It has a smooth oil-lubricated carriage to allow for accurate measurements of turbulent velocity, temperature, and salinity fluctuations, and the carriage can be used to tow the terrain model in the tank.
- 4) It has a mini-computer system for direct on-line data acquisition and analysis. The mini-computer system can handle a maximum data rate of 44,000 samples per second at 13 bits accuracy. The system has a memory core of 20,000 words and a disc storage of 2.5 million words at 16 bit accuracy. In conjunction with this mini-computer system, a series of computer programs has been developed to obtain statistical moments up to fourth-order.

3.2 The Terrain Model and Platform

A terrain model was made of polyurethane foam (9.6 Kg/m^3 density) mounted on a $3.66 \text{ m} \times 1.14 \text{ m} \times .64 \text{ m}$ acrylic plastic sheet reinforced with aluminum angles and bars on the back side. The mountain terrain section was interchangeable with a flat surface. The surface of the plastic sheet was covered with a sheet of .64 cm polyurethane foam. The foam surface was studded with artificial roughness elements, .32 cm in diameter and having an average height of .32 cm, with a density of about 1 element/cm². The entire model was painted flat white to improve photographic quality.

The vertical profile $h(x,y)$ of the terrain model is described by the sum of three Gaussian functions

$$h(x,y) = a_0 \{ \exp[a_1(x-x_0)^2 + a_2(y-y_0)^2] + \exp[a_1(x-x_0)^2 + a_2(y+y_0)^2] \} \\ + a_3 \{ \exp[a_4(x-x_0)^2 + a_5y^2] \} , \quad (3.1)$$

where the coordinates are referenced to the stack base. The following coefficients, $a_0 = 17.80$, $a_1 = -.0008513$, $a_2 = -.01197$, $a_3 = 16.0$, $a_4 = -.01171$, $a_5 = -.002314$, $x_0 = 61$, and $y_0 = 18.82$ (length dimension in cm) were selected. The terrain model had the essential features of a complex terrain, namely, mountains, mountain ridges, and valleys. Cross-sectional views of the terrain model are plotted in Fig. 2; and contour map is plotted in Fig. 3. The characteristic length scales of the terrain and the stack are summarized in Table 1.

In the stratified towing tank, the terrain model and the stack were actually mounted upside down under the oil-lubricated carriage, and the effluent, heavier than the ambient fluid at the stack exit, was injected downwards from the stack exit into a stably or neutrally stratified fluid. The terrain model was towed at a speed specified for a particular experiment. This arrangement was used to simulate the hot effluent rising upwards from a stack into a stable or a neutral atmosphere.

3.3 The Effluent Injection Device

Concentrated salt (NaCl) solution was used as the effluent fluid. The effluent device consisted of a pressurized storage chamber for the salt solution, a portable tank of compressed air, a needle valve for regulating the effluent discharge, and a flow meter for measuring the flow rate. A dye container filled with a blue food dye was inserted between the flow meter outlet and the stack. The stack was made of stainless steel tubing with an inside diameter of .318 cm. The effluent flow was tripped with a small ring (.16 cm I.D.) installed inside the tubing about 1 cm from the stack exit, and the plume was fully turbulent at the stack exit. Figure 4a shows the effluent injection device.

To measure pollutant concentrations on the terrain surface, temperature was used as a tracer. The plume was heated by a portable boiler, which was made of a stainless steel filter case (Cat. No. BRX10-3/4B, Commercial

Filter Corporation) wrapped with a 400 watts heating tape (Cat. No. 33745-120, Van Waters and Rogers, Inc.), and was connected to the effluent feeding line between the dye container and the stack. By adjusting a voltage regulator (a Variac Transformer) connected to the heating tape, the plume temperature could be controlled. The temperature of effluent at the stack exit was measured with a 10 gauge thermo-couple probe (SCXSS-010G-36" T/C Omega Engineering, Inc.) inserted inside the stack. The plume temperature was kept at $77^{\circ}\text{C} \pm 2^{\circ}\text{C}$ for ground concentration measurements.

3.4 Flow Visualization Techniques

Shadowgraph and dye methods were used to visualize the plume dispersion in stratified and nonstratified fluids. Since the shadowgraph intensity is directly proportional to the second derivatives of the refraction index, the small structure of turbulent motions in a plume of a salt solution and in the turbulent boundary layer of the stratified flow over the terrain surface can be visualized from shadowgraph pictures. For the present experiments, a parallel light beam of diameter 30.5 cm was obtained by projecting a point light source at the focal point of a parabolic mirror of 30.5 cm in diameter and 2.5m in focal length. A Xenon-Mercury D.C. light source (1000 watts) equipped with condensing lens and pin-holes was used as the point light source. When a parallel light beam passes through the turbulent stratified plume, a shadowgraph is produced.

Dye visualization methods were used to visualize the large scale plume motions and to trace the plume. Movie and still cameras were used to record visualization data during the experiments.

3.5 Hot-Film Anemometer, Conductivity Gauge, and Temperature Gauge

The mean and fluctuating velocities in the plume were measured with a 10-channel constant temperature anemometer (Model 1051-10, Thermo-Systems, Inc.) using conical and cylindrical hot-film probes (TSI Model 1230S and 1290AK) as sensors. The anemometer has a frequency response up to 1 KHz. Figure 5a shows a typical velocity calibration curve plotted as the output voltage vs velocity. The sensitivity is about 2 volts per cm/sec.

Flow Research has developed a fast response temperature gauge which measures resistance changes of a metallic film corresponding to variations of the fluid temperature. The gauge employs the sensor as one arm of a balanced bridge driven by a 10 KHz oscillator which supplies a low current (several MA) to the bridge. The bridge is initially balanced by means of an adjustable resistor. As the resistance of the sensor varies, the signal of imbalance modulates the 10 KHz carrier frequency, and is then amplified and synchronously detected.

Cylindrical hot-film probes (TSI Model 1290AK) were used as the sensors which had a temperature coefficient of $.0026 \Omega/^{\circ}\text{C}$ and a natural frequency (thermal) of 850 Hz. A calibration circuit which changes the current through one side of the bridge by .26% (equivalent to 1°C temperature change) was built in the gauge. The output of the bridge during calibration was 15Hz square waves whose peak-to-peak amplitude corresponded to a 1°C temperature change. The linearity of the gauge was within 0.1%. The temperature gauge was calibrated against a mercury thermometer with $.1^{\circ}\text{C}$ increment in the water bath. A typical temperature calibration curve is shown in Figure 5 b ; the sensitivity is about $1.5 \text{ V}/^{\circ}\text{C}$. The equivalent noise level in temperature measurements was $.004^{\circ}\text{C}$.

Ten conductivity gauges (Model 1110) developed by Flow Research, Inc. were used to measure density profiles in the plume. This gauge has a frequency response from DC to 1 KHz. The sensor was a single electrode conductivity probe which had a .025 mm stainless steel tip platinized with platinum black solution. The sensitivity of the conductivity gauge is about 1 volt per $0.025 \text{ gm}/\text{cm}^3$. Figure 6 a shows a typical calibration curve of the conductivity probe where Σ is a reduced fluid density defined as $\Sigma = (\rho - 1) \times 1000$, where ρ is the specific gravity of the fluid. Figure 6b is a typical density profile which has a fairly constant gradient over about 60 cm. The experiments were conducted at a depth of about 15 cm below the water surface.

4. Flow Visualizations

4.1 Plume Dispersion in Stratified and Nonstratified Flows over a Flat Plate

The plume spreads ($R_D = 530$) in stagnant nonstratified ($F_D = 2.84$) and stratified fluids ($F_D = 2.92$) were observed with shadowgraph pictures shown in Figs. 7a and 7b. The plume in a nonstratified fluid spreads continuously as it rises. The plume in a stratified fluid ($N = 0.14$ cycle/sec) spreads in the initial stage as the plume in a nonstratified fluid does, but in the stratified fluid, the plume rise is limited. The shadowgraph shows that the plume spreads outward in horizontal directions after it reaches its terminal rise. The plume is turbulent except in the outer region of the spreading disc.

The entrainment coefficient α was measured using $R = 2\alpha Z$, where R is the radius of visible plume boundary, and has a value $\alpha = 0.08$. The entrainment coefficient observed by the others, are, $\alpha = 0.093$ by Morton, et al. (1956), $\alpha = 0.075$ by Briggs (1968), and $\alpha = 0.08$ by Ricou et al. (1961).

The dispersion of bent-over plumes ($K = 1.7$, $R_D = 530$) in nonstratified ($F_D = 2.84$) and stratified ($F_D = 2.92$) flows is shown in Figs. 8a and 8b. The corresponding internal Froude numbers $F_H = U_\infty/NH$ are ∞ and 1.69, respectively. The bent-over plume in a nonstratified flow is turbulent and spreads continuously as it rises. The shadowgraph picture shows that the upper boundary of the plume is rougher than the lower boundary because inside the plume the mean density stratification is unstable in the upper half of the plume and is stable in the lower half.

Figure 8b shows that both the plume and the boundary layer, which has a thickness about 2.5 cm, in the stratified case are turbulent. In the near downstream of the stack, the plume in the stratified flow spreads and rises. But further downstream, the plume reaches a terminal height and the vertical spread is limited. The trajectories of plumes, which are defined as the mid-point of the upper and lower plume edges, are determined by averaging five ensembles. They are plotted as ZU_∞^3/F vs xU_∞^3/F in Fig. 9, where F is the buoyancy flux of the plume defined by $F = W_s(\rho_s - \rho_a)gD^2/4\rho_a$.

The plume in a nonstratified flow rises continuously and its trajectory is correlated by the equation

$$\frac{ZU_\infty^3}{F} = 1.6 \cdot \left(\frac{xU_\infty^3}{F} \right)^{2/3} \quad (4.1)$$

or

$$\frac{Z}{D} = 1.6 K F_D^{-2/3} \left(\frac{x}{D} \right)^{2/3}. \quad (4.2)$$

The coefficient in the right hand side of Eq. (4.1) was observed to be 1.8 by Briggs (1969), 1.44 by Hewett, et. al. (1970), and 1.6 by Turner (1973). In the stratified flows, the vertical rise of plumes is limited by the stable stratification, and the plume oscillates with x after its maximum rise is reached.

Trajectories of plumes in stratified flows are re-plotted as $Z/(F/U_\infty s)^{1/3}$ vs $x/(U_\infty s^{-1/2})$ in Fig. 10, where s is the stability parameter defined by $s = (2\pi N)^2$. Other laboratory data (Hewett et al. 1970) and field data from TVA plants (see Briggs 1969) are also plotted in Fig. 10. For high F_H , the maximum plume rise occurs at about $x/(U_\infty s^{-1/2}) = 4$ or $Nx/U_\infty = 0.65$, and the terminal plume trajectory has a height about 2.2. When F_H decreases, the plume rise increases as possibly the result of the reduction of cross-flow entrainment with increasing stability. This could explain partially for the scatter of the field data plotted in Fig. 10.

The laboratory and field data of terminal plume rise in stratified flows are plotted as Z_t vs $5 F^{1/5} S^{-3/8}$ in Fig. 11. The terminal plume rise is defined as the final height of the plume top. Our experimental data of the plumes in stagnant stratified fluids ($F_H = 0$) and in stratified flows ($F_H = 3.11$ and 6.22) are in good agreement with the data obtained by the others (Briggs 1969). The agreement shown in Figs. 10 and 11 would then support the arguments (Section 2) that the stack Reynolds number need not be simulated critically in a stably stratified flow as long as the plume is turbulent at the stack exit.

The vertical and lateral spreads of plumes in a nonstratified flow over a flat plate are plotted as $\Delta Z U_\infty^3/F$ and $\Delta Y U_\infty^3/F$ in Figs. 12 and 13, respectively, where the plume spreads are determined by averaging 5 ensembles. The vertical and lateral spreads are correlated by

$$\frac{\Delta Z U_{\infty}^3}{F} = 1.25 \left(\frac{x U_{\infty}^3}{F} \right)^{2/3}, \quad (4.4)$$

and

$$\frac{\Delta Y U_{\infty}^3}{F} = 1.5 \left(\frac{x U_{\infty}^3}{F} \right)^{2/3} \quad (4.5)$$

in the range $\frac{x U_{\infty}^3}{F} > 6$. The lateral spread is greater than the vertical spread, and the aspect ratio of the plume cross section is about 1.2. A top view of a dyed plume in a nonstratified flow is shown in Fig. 14 a. The plume appears to split into two parts, which indicates the formation of the twin vortex. The twin vortex has been observed in the field under some conditions (Scorer, 1968).

Figures 12 and 13 show the vertical and lateral spreads of plumes in stratified flows. In the region where the buoyancy dominates the plume rise, Eq. (4.5) provides the limiting spreads of the plume in stratified flows. The vertical spread is limited by the stable stratification and appears to oscillate with x after it reaches its maximum value. A top view of a dyed plume in a stratified flow ($F_H = 6.22$) is shown in Fig. 14 b. The twin-vortex structure is not observed because the vertical motion of the twin vortex is suppressed in a stratified flow.

4.2 Plume Dispersion in a Stratified Flow over the Terrain Model

A side view and a top view of a dyed plume at $F_D = 3.16$, $K = 6.8$, and $R_D = 530$ in a stratified flow ($F_h = 0.97$) over the terrain model are presented in Fig. 15. The flow direction was from right to left at $U_{\infty} = 3$ cm/sec. The stack was located at $x/D = 192$ upstream of the ridge between the two mountain peaks. The plume appears to be fully turbulent and tends to relaminarize as it levels off. Before the plume levels off, it tends to overshoot. The residue momentum of the plume which dissipates as the entrainment process progresses, initiates the overshooting. Further downstream, the plume remains aloft in both upstream and downstream sides of the terrain. The top view of the dyed plume shows the spread of the plume in the lateral direction. The pollutant accumulation is seen around the I-shaped bright area (Fig. 15 b), which corresponds to the two mountain peaks and the ridge between them (See Fig. 3).

The effects of the flow speed on the plume dispersion over the terrain were examined by increasing the flow speed from $U_{\infty} = 3$ cm/sec to 6 cm/sec but leaving the other flow conditions unchanged (Figs. 16 a and 16 b). When the wind speed increases, the plume bends more toward the downwind side of the stack, and the overshoot of the plume becomes less pronounced. Further, in the lee side of the mountain ridge, the plume is carried toward the ground surface by the downslope flow resulting from the increase in flow speed.

Two additional cases with weaker stratifications ($N = .14$ cps) than those described above are shown in Figs. 17 and 18. It can be readily observed that the terminal rise increases with decreasing stability while the gross features of the plumes remain unchanged.

The terrain effects are investigated by comparing the vertical and lateral boundaries of a plume over the terrain with those of a plume over a flat plate (Fig. 19). With the presence of an obstacle, the stably stratified flow upstream is blocked. Velocity profiles presented in Section 5 indicate that the upstream blocking extends beyond the distance where the stack is located. The upstream blocking which reduces the mean advection speed U_a at the stack exit effectively increases the local speed ratio W_s/U_a . As a result, the plume rise increases with increasing blocking.

In a stably stratified flow, a semi-stagnant or plugged region (Turner 1973) usually develops just upstream and below the obstacle. The accumulation of pollutants observed in Fig. 16 confirms the existence of such a region.

When the obstacle is three-dimensional as is the terrain model used in the experiments, the stably stratified fluid tends to flow around rather than over the obstacle because the vertical motion is inhibited. The induced lateral current carries a portion of the pollutants around the mountain peaks and therefore effectively enhances the lateral spread of the plume as observed in Fig. 19.

Plots of the plume trajectories and the plume spreads $\Delta Z/D$ and $\Delta Y/D$ vs Nx/U_{∞} are presented in Figs. 20, 21, and 22, respectively. The rise and the spreads for plumes over the terrain model are always greater than those over the flat plate provided that the induced lateral current is relatively small. Under such a circumstance, the upstream blocking contributes mainly to the increase of the rise and the

spreads. As the plume approaches the mountain ridge, the induced lateral current becomes pronounced. It increases the lateral spread considerably and consequently reduces the vertical spread as can be seen in Fig. 22. Both the maximum rise and the maximum vertical spread tend to occur about $Nx/U_\infty = .65$ whether the flow is over the terrain model or over the flat plate. Apparently, these two features only depend on the buoyancy of the plume and the stability of the ambient fluid.

The dispersion of bent-over plumes from a stack located downstream of the ridge was also investigated. Figure 23 a shows a dyed plume released from a stack $F_D = 2.09$ and $F_h = 1.32$. The plume rises straight upwards and spreads horizontally in both upstream and downstream directions, as the maximum rise is reached. However, at a higher internal Froude number $F_h = 2.64$ (Fig. 23b), the plume is bent over toward the downstream direction and is carried downstream by the downslope flow. The formation of lee waves traced by the dispersing plume and the turbulent layer near the ground surface can be clearly observed in Fig. 23b.

5. Velocity, Density and Pollutant Concentration Measurements

The turbulent plume in a stratified flow was investigated by measuring the velocity and density profiles in the plume from a stack which was located in the valley and at $192 D$ upstream from the ridge between the mountain peaks. The stack exit was at an elevation $x/D = 16$, and the mountain ridge had a height $h/D = 510$. The free stream velocity U_∞ was 6 cm/sec , the Brunt-Vaisala frequency was $N = .14 \text{ cycle/sec}$, and the internal Froude number was therefore $F_h = U_\infty/N_h = 2.64$. The stack Froude number F_D was 3.09 , the velocity ratio K was 3.4 , and the stack Reynolds number was $R_D = 530$.

The conductivity probes were aligned vertically at the plume axis and the hot-film probes were 1 cm away from the plume axis (see Fig. 4b). The velocity and density measurements were conducted at three downstream stations from the stack, $x/D = 32, 64, \text{ and } 96$. The plume trajectories indicated by the position of the maximum velocity intensity $\sqrt{u^2_{\max}}$ and by the maximum density fluctuation $\sqrt{\sigma^2_{\max}}$ are plotted in Fig. 24. They are in fair agreement with the plume trajectory determined from dye visualizations.

The mean velocity profiles \bar{U}/U_∞ in the upstream of the terrain ridge are plotted vs z/D for $x/D = 32, 64, 96$. The significant variations in the velocity in the vertical direction is probably not caused by the boundary layer but rather by the terrain because the turbulent boundary layer has a thickness only of about $10 D$. Further, the velocity varies significantly with the distance from the mountain ridge and the effects of terrain on a stably stratified flow (upstream blocking) are therefore clearly demonstrated.

The maximum values of the longitudinal velocity intensity $\sqrt{u^2_{\max}}/W_s$ at 3 downstream positions are plotted vs x/D in Fig. 26. The decay of velocity intensity is approximated by

$$\sqrt{u^2_{\max}}/W_s = 2.8 (x/D)^{-1}. \quad (5.1)$$

The maximum values of the density intensity $\sqrt{\sigma^2_{\max}}/\Sigma_s$ are also plotted vs x/D in Fig. 26 where $\Sigma_s = (\rho_s - 1) \times 1000$ is the reduced density of the effluent at the stack exit and σ is the turbulent fluctuation of the reduced density. The maximum density intensity decays in the range $30 < x/D < 60$ but increases instead at $x/D = 96$.

The normalized velocity intensities $\sqrt{u^2}/\sqrt{u_{\max}^2}$ are plotted vs $2(z-Z_u)/\Delta Z_u$ in Fig. 27 where Z_u is the vertical coordinate of the maximum velocity intensity, ΔZ_u is the width between the plume boundaries at which the velocity intensity is half of its maximum. The normalized profiles are not symmetric with the plume trajectory but approximately self-similar. Also plotted in Fig. 27 are the normalized density intensities $\sqrt{\sigma^2}/\sqrt{\sigma_{\max}^2}$ vs $2(z-Z_\sigma)/\Delta Z_\sigma$ where Z_σ is the vertical coordinate of the maximum intensity of density fluctuations, and ΔZ_σ is the width between the boundaries at which the intensity of density fluctuations is half of its maximum.

The flatness factor of the velocity fluctuations $\overline{u^4}/(\overline{u^2})^2$ is plotted vs $2(z-Z_u)/\Delta Z_u$ in Fig. 28a. Inside the plume the flatness factor has an average value of about 2.8, and near the plume boundary, the flatness factor has a sharp variation. The flatness factor of the density fluctuations $\overline{\sigma^4}/(\overline{\sigma^2})^2$ is plotted vs $2(z-Z_\sigma)/\Delta Z$ in Fig. 28b and it has an average value of about 3 inside the plume but has a sharp variation near the plume boundary. It is noted here that it has been observed from the velocity and density measurements in a turbulent wake in a stratified fluid (Pao et al. 1973, and Lin et al., 1973) that the flatness factor remains fairly constant inside the wake but has a sharp variation near the wake boundary.

The pollutant concentrations on the ground level of the terrain were measured using temperature as a tracer. The locations of the five ground stations on the upwind slope of the terrain are shown in Fig. 3 and are summarized in Table 2 where x, y, and z are the coordinates referenced to the stack base. The stack Froude number was $F_D = 3.16$, the stack Reynolds number was $R_D = 530$, and the plume temperature at the stack exit was $\theta_s = 77 \pm 2^\circ\text{C}$. The ambient fluid was stratified with a Brunt-Vaisala frequency $N = 0.14$ cycle/sec, and the ambient temperature was $\theta_a = 19^\circ\text{C}$. The towing speeds were at $U_\infty = 3$ cm/sec and 6 cm/sec, and the corresponding internal Froude numbers were $F_D = 1.32$ and 2.64, respectively. The mean and rms pollutant concentrations determined from the mean and rms temperature measurements are tabulated in Table 2b. For $F_h = 1.32$, the mean concentration at the station 1 is the highest and the rms concentration at all stations is not significant. However, as F_h increases to 2.64, the mean concentration at station 1 is three times reduced but the rms concentration increases by a factor of about 9. For the terrain investigated here, the highest pollutant concentration (mean and rms) always occur at the mountain ridge.

6. Conclusions

i. The fair agreement among the present results of plumes over a flat plate in the towing tank and other laboratory and field data (Figs. 10 and 11) suggests that the stack Reynolds number R_D need not be critically simulated for plume dispersion in a stable atmosphere. It is required, however, that the plume should be turbulent at its exit for a correct simulation in both the near and the far fields.

ii. With the presence of the three-dimensional terrain model, the stably stratified flow ($F_h = 1$ to 3) upstream of the mountain ridge is blocked. The velocity data (Fig. 25) verify the existence of the upstream blocking. As a result, the plume rise and spread increase because the local speed ratio W_s/U_a increases. In one case (Fig. 16), a significant amount of pollutants is trapped in the semi-stagnant region just upstream of and below the mountain ridge.

iii. The stably stratified fluid tends to flow around rather than over the terrain model because the vertical motion is inhibited. Near the mountain ridge, the induced lateral current is pronounced. The lateral spread increases considerably and consequently the vertical spread reduces.

iv. At a small Froude number ($F_h = 1.32$) the pollutants carried around and over the terrain model remain aloft. As the Froude number increases ($F_h = 2.64$), pollutants downstream of the terrain model are carried closer to the ground surface by the downslope flow.

v. When the stack is located in the lee side of the terrain model, the trajectory or the plume is strongly governed by the internal Froude number. For small F_h (approx. 1.32), the plume spreads into both the upstream and downstream sides of the stack because the flow field adjacent to the downstream side of the mountain ridge is nearly stagnant. However, at a higher Froude number ($F_h = 2.64$), the plume is advected downstream by the downslope flow.

vi. The plume trajectories determined as the loci of the maximum rms velocity and rms density in the plume are in fair agreement with that determined from the visualization results.

vii. The rms velocity and rms density profiles normalized by the respective maximum values are not symmetric with the plume trajectory. These profiles

(Fig. 27) plotted against the height normalized by the respective half radii, appear to be approximately self-similar. The normalized flatness factor of the velocity and density fluctuations in the plume (Fig. 28) are also approximately self-similar. The flatness factors remain almost constant but have a sharp variation across the plume boundary.

viii. The pollutant concentrations in the upstream surface of the terrain were measured by using temperature as the tracer. The mean and rms concentrations at stations in the mountain ridge are higher than those at other stations.

7. References

- Briggs, G. A. (1968). "Penetration of Inversions by Plumes", Paper presented at 48th Annual Meeting of the American Meteorology Society, San Francisco.
- Briggs, G. A. (1969). Plume Rise, U.S. Atomic Energy Commission Critical Review Series, TID-25072.
- Bringfelt, B. (1968). "Plume Rise at Industrial Chimneys," Atmospheric Environment, 2, 575-598.
- Fay, J. A., M. Escudier, and D. P. Hoult (1969). "A Correlation of Field Observations of Plume Rise", Fluid Mech. Lab. Publication No. 69-4, Dept. of Mech. Engineering, MIT.
- Hewett, T. A., J. A. Fay, and D. P. Hoult (1970). "Laboratory Experiments of Smokestack Plumes in a Stable Atmosphere", Fluid Mech. Lab., Dept. of Mech. Engineering, MIT.
- Hino, M. (1968). Computer Experiment on Smoke Diffusion over a Complicated Topography. Atmospheric Environment, 2, 541-558.
- Hoult, D. P., and J. W. Weil (1972). "Turbulent Plume in a Laminar Cross Flow", Atmospheric Environment, 6, 513-531.
- Lin, J. T., and Y. H. Pao (1973). "Velocity and Density Measurements in the Turbulent Wake of a Self-Propelled Slender Body in Stratified and Nonstratified Fluids", Flow Research Report No. 14, Kent, Washington
- Morton, B. R., G. I. Taylor, and J. S. Turner (1956). "Turbulent Gravitational Convection from Maintained and Instantaneous Sources". Proc. Roy. Soc. London, A234, 1-23.
- Orgill, M. M., J. E. Cermak, and L. O. Grant (1970). "Laboratory Simulation and Field Estimates of Atmospheric Transport-Dispersion over Mountainous Terrain," Technical Report CER70-7LMMO-HFC-LOG40, Colorado State University.
- Pao, Y. H., J. T. Lin, R. L. Carlson, and L. P. C. Smithmeyer (1971). "The Design and Construction of a Stratified Towing Tank with an Oil-Lubricated Carriage". Flow Research Report No. 4, Kent, Washington.
- Pao, Y. H., and J. T. Lin (1973). "Velocity and Density Measurements in the Turbulent Wake of a Towed Slender Body in Stratified and Nonstratified Fluids", Flow Research Report No. 12, Kent, Washington.
- Ricou, J. P. and D. B. Spalding (1967). "Measurement of Entrainment by Axialsymmetrical Turbulent Jets", J. Fluid Mech., 11, 21-32.

Slade, D. H. (1969). "Low Turbulence Flow in the Planetary Boundary Layer and Its Relation to Certain Air Pollution Problems", J. of Applied Meteorology, 8, 514-522.

Scorer, R. S. (1968). Air Pollution, Pergamon Press, London.

Turner, J. S. (1973). Buoyancy Effects in Fluids, Cambridge University Press.

Veenhuizen, S. D., J. T. Lin, Y. H. Pao, D. W. Peecher and G. L. Hiatt. (1973). Laboratory Simulation of Plumes From Kennecott Copper Smelters in Garfield, Utah: Neutral Atmosphere. Flow Research Report No. 9, Kent, Washington.

TABLE 1. STACK AND TERRAIN LENGTH SCALES

Scale factor 1:2,500

Descriptions	Prototype	Model
Stack Diameter D	7.94 (m)	.32 (cm)
Stack Height H	127.0 (m)	5.08 (cm)
Mountain Peaks Height h_o	609.6 (m)	24.38 (cm)
Mountain Peak Separation	941.0 (m)	37.64 (cm)
Mountain Ridge Height h	406.4 (m)	16.26 (cm)

Table 2 SUMMARY OF GROUND SURFACE TEMPERATURE MEASUREMENTSa. Coordinates of Ground Stations

<u>Station</u>	<u>x(cm)</u>	<u>y(cm)</u>	<u>z(cm)</u>
1	61.0	0	16.3
2	56.3	0	12.7
3	53.8	0	8.9
4	61.0	6.4	16.3
5	56.3	6.4	12.7

b. Experimental Data

<u>Station</u>	$F_h = \frac{U_\infty}{Nh}$	$\theta_s (^{\circ}C)$	$\theta_a (^{\circ}C)$	$\theta (^{\circ}C)$	$\frac{\theta - \theta_a}{\theta_s - \theta_a}$	$\frac{\sqrt{\theta^2}}{\theta_s - \theta_a}$
1	1.32	77	19.55	19.76	3.7×10^{-3}	7.0×10^{-5}
2	1.32	77	19.55	19.58	5.2×10^{-4}	1.2×10^{-4}
3	1.32	77	19.55	19.58	5.2×10^{-4}	1.7×10^{-5}
1	2.64	77	20.65	20.73	1.4×10^{-3}	6.0×10^{-4}
2	2.64	77	20.65	20.68	5.3×10^{-4}	1.6×10^{-4}
3	2.64	77	20.65	20.70	8.9×10^{-4}	1.1×10^{-4}
4	2.64	77	20.38	—	—	4.9×10^{-4}
5	2.64	77	20.38	20.40	3.5×10^{-4}	1.4×10^{-4}

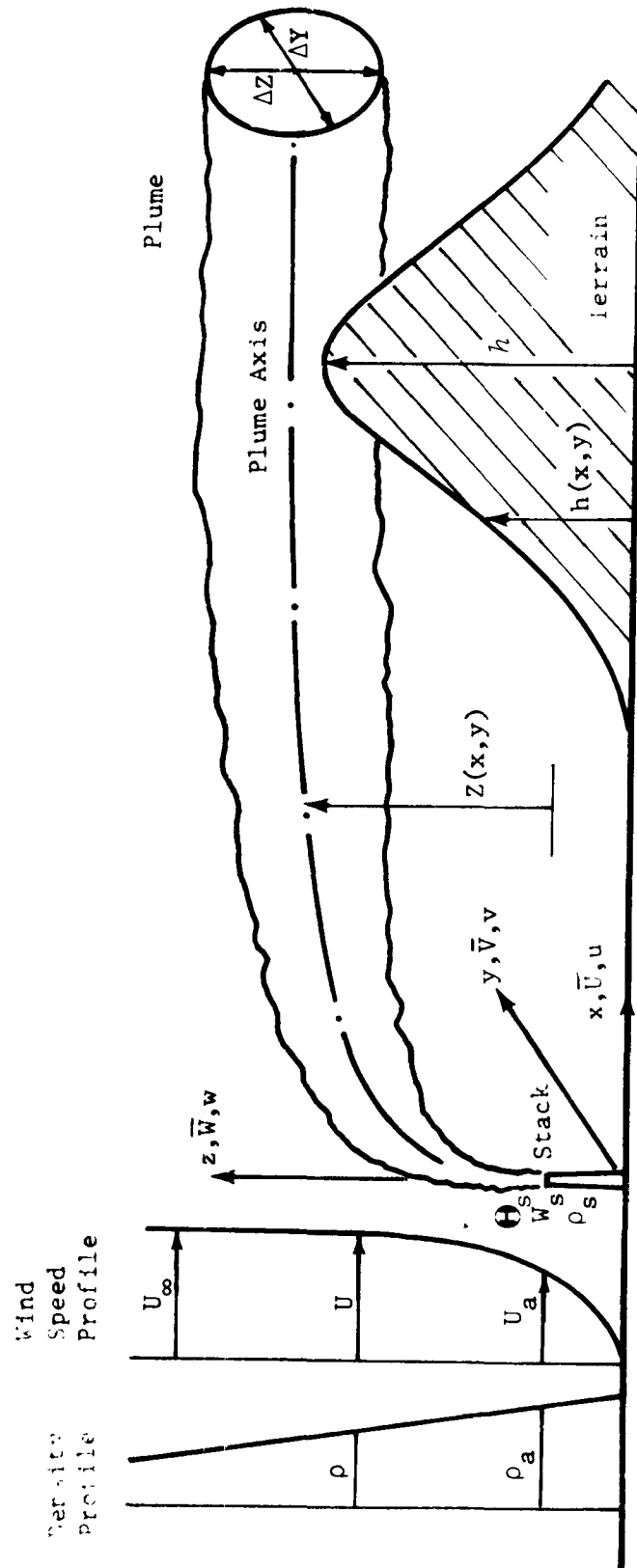


Figure 1. Definition Sketch

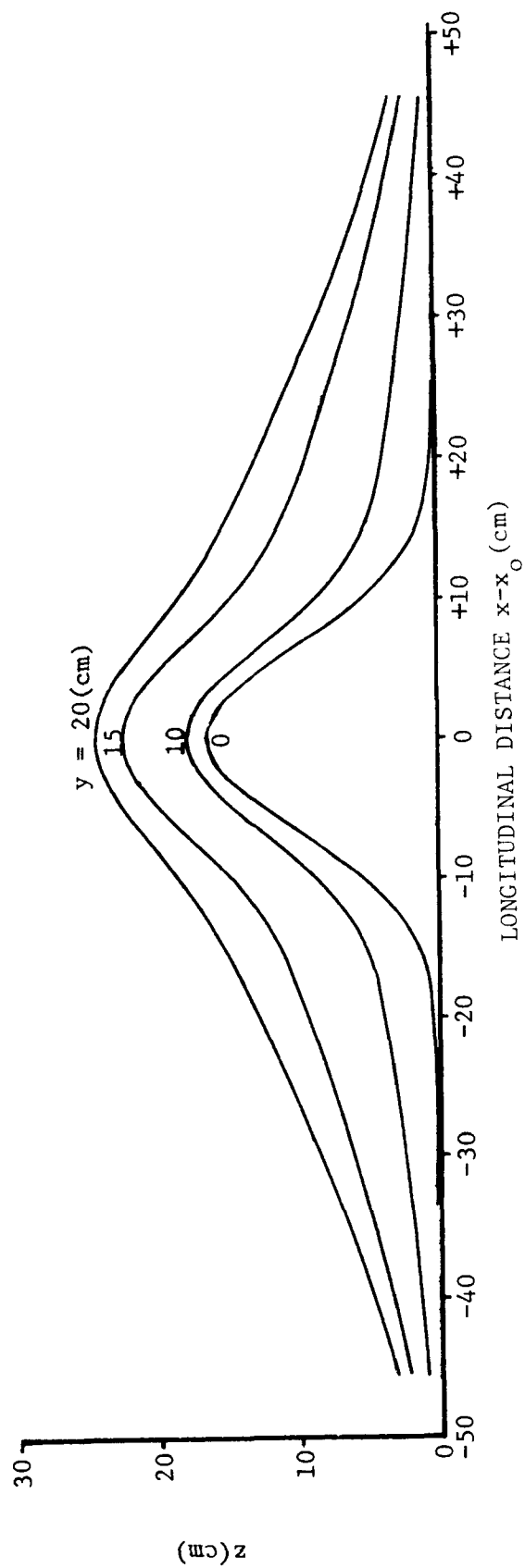
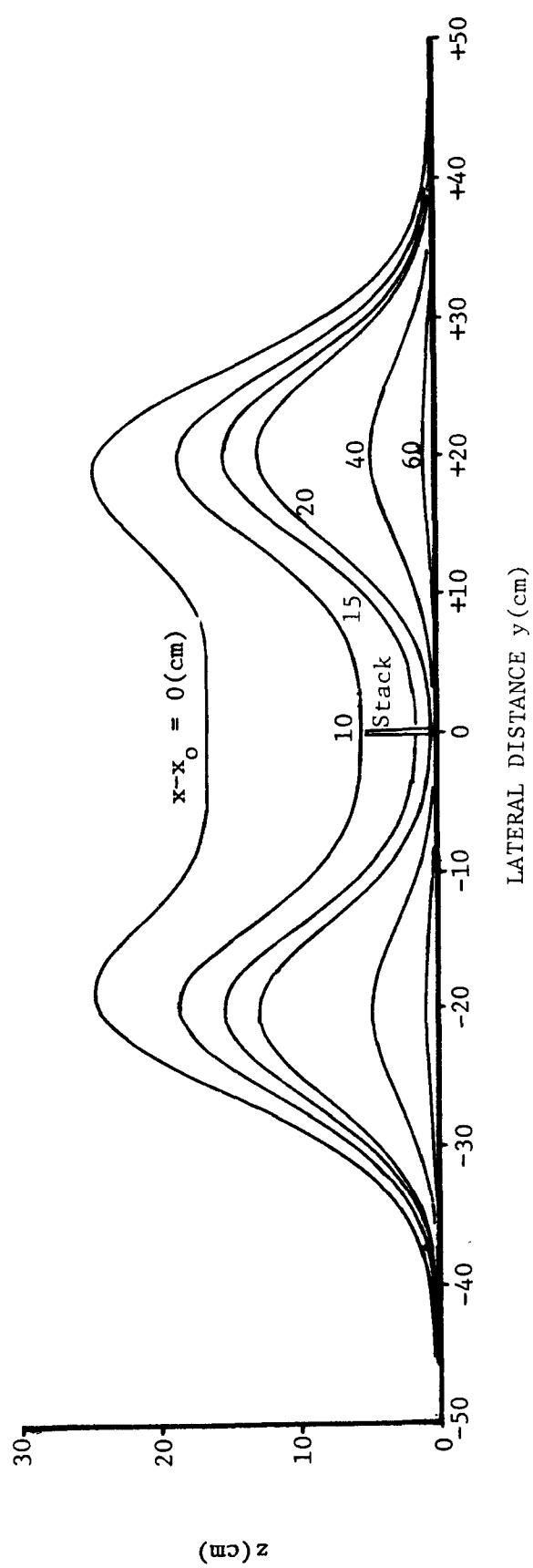


Figure 2. Cross-sectional Views of the Terrain Model.

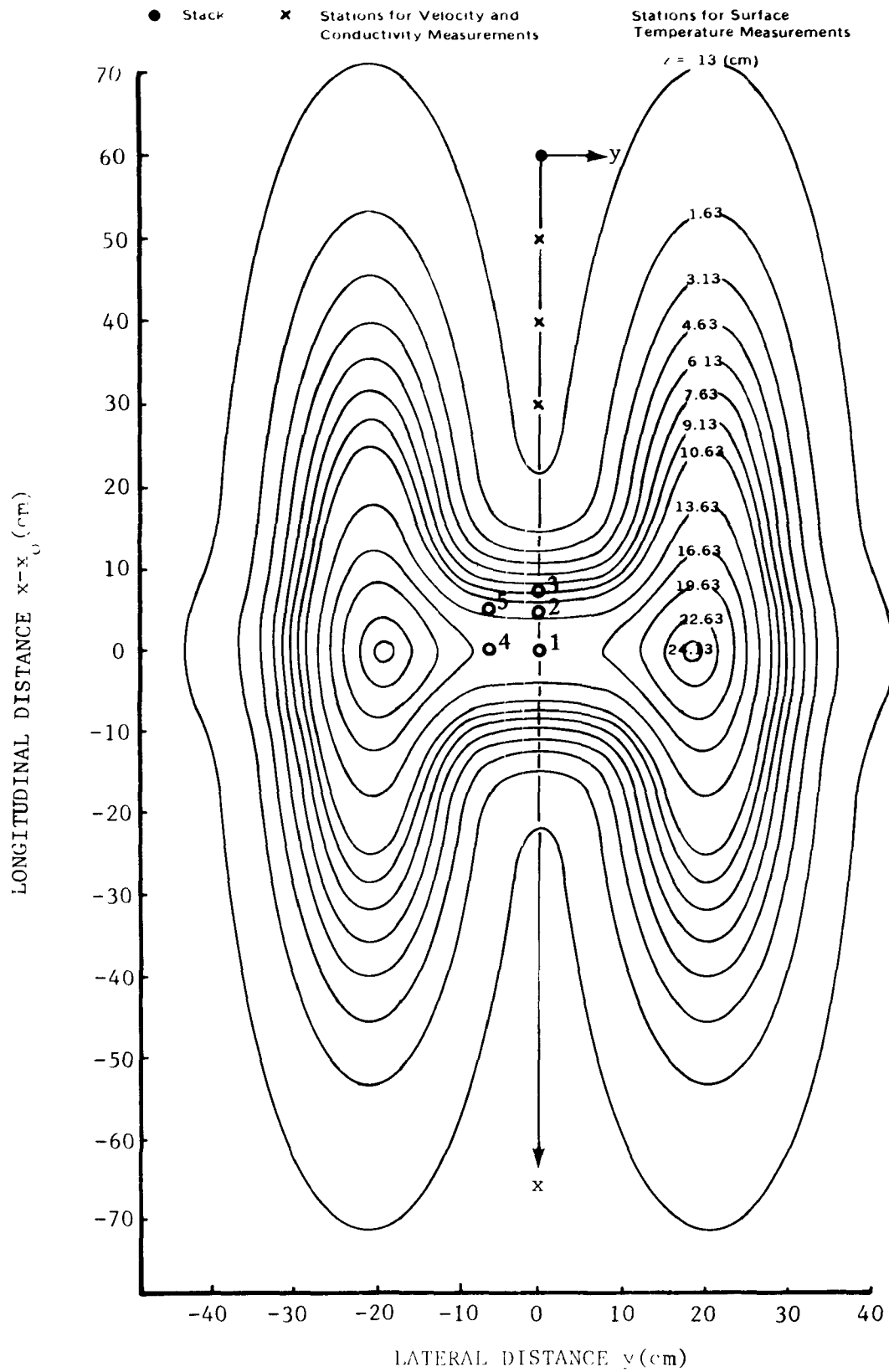
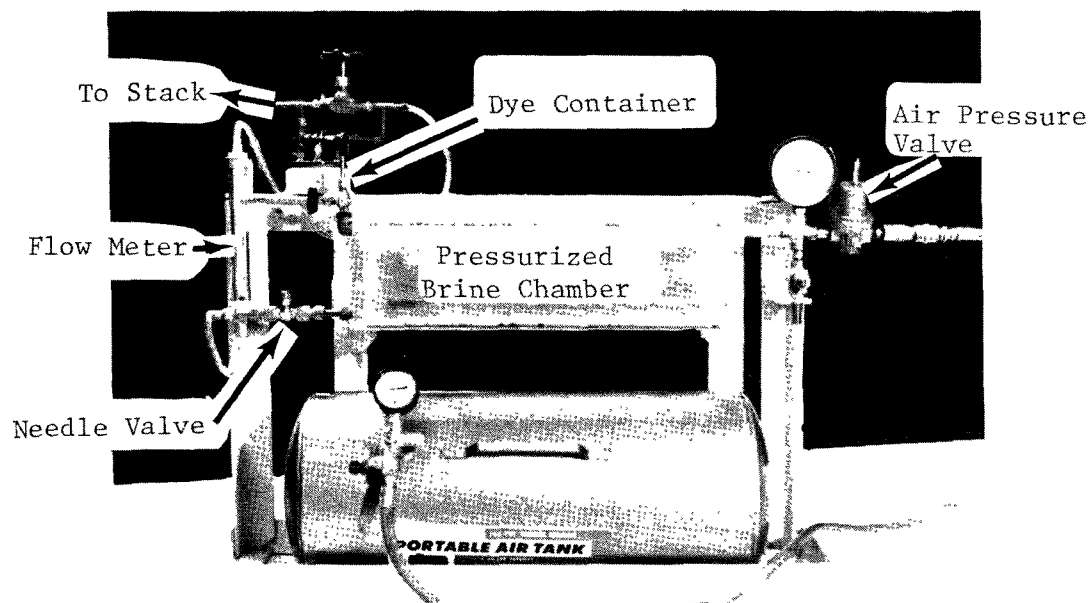
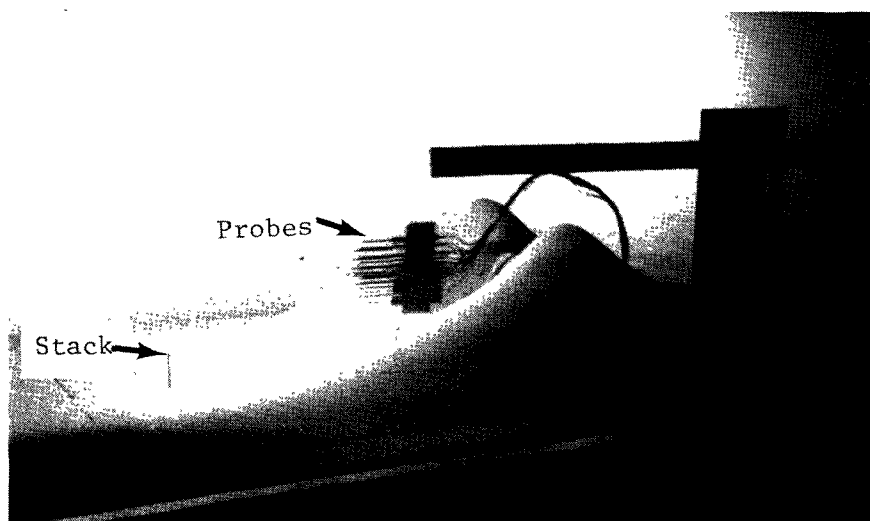


Figure 3. A Contour Map of the Terrain Model

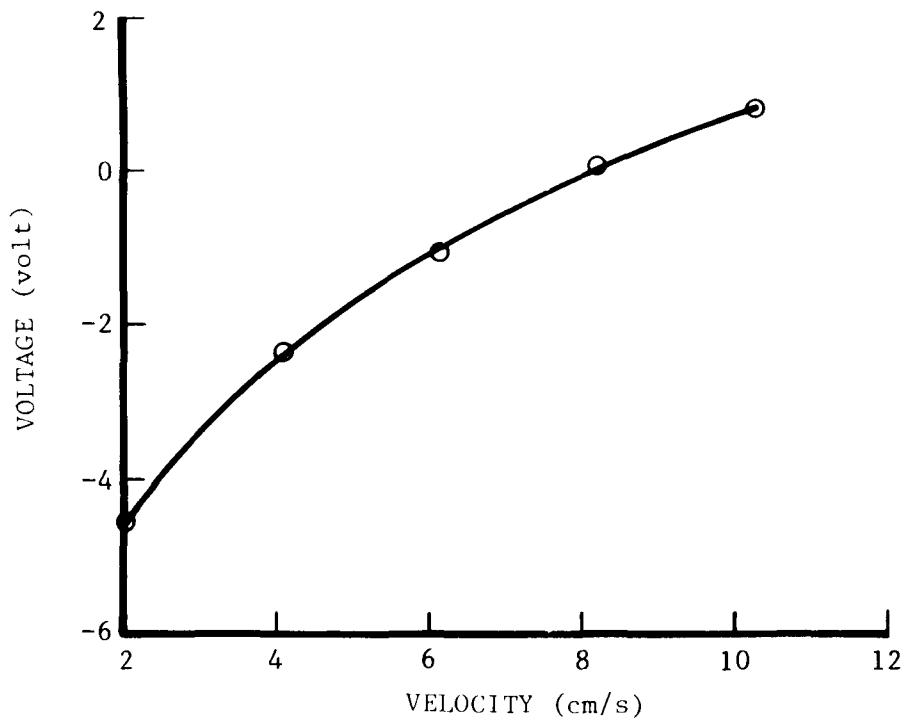


a. Effluent Injection Device

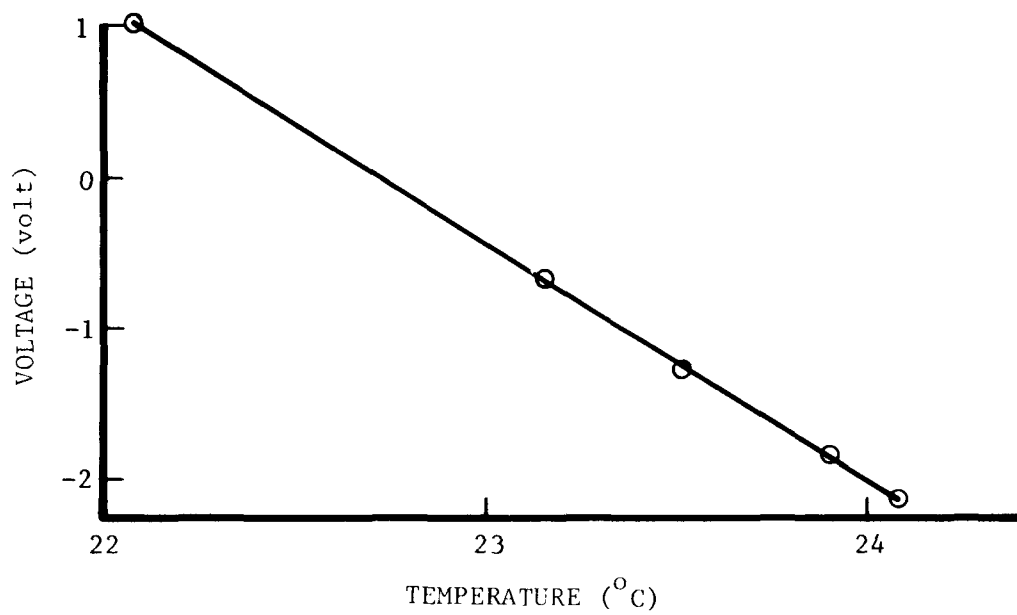


b. Experimental Set-up for Velocity and Conductivity Measurements

Figure 4. The Effluent Injection Device and Arrangement for Probe Measurements



a. Velocity Calibration of a Hotfilm Probe with a Constant Temperature Anemometer



b. Temperature Calibration of a Thinfilm Probe with a Temperature Gauge

Figure 5. Typical Calibrations of Velocity and Temperature Probes

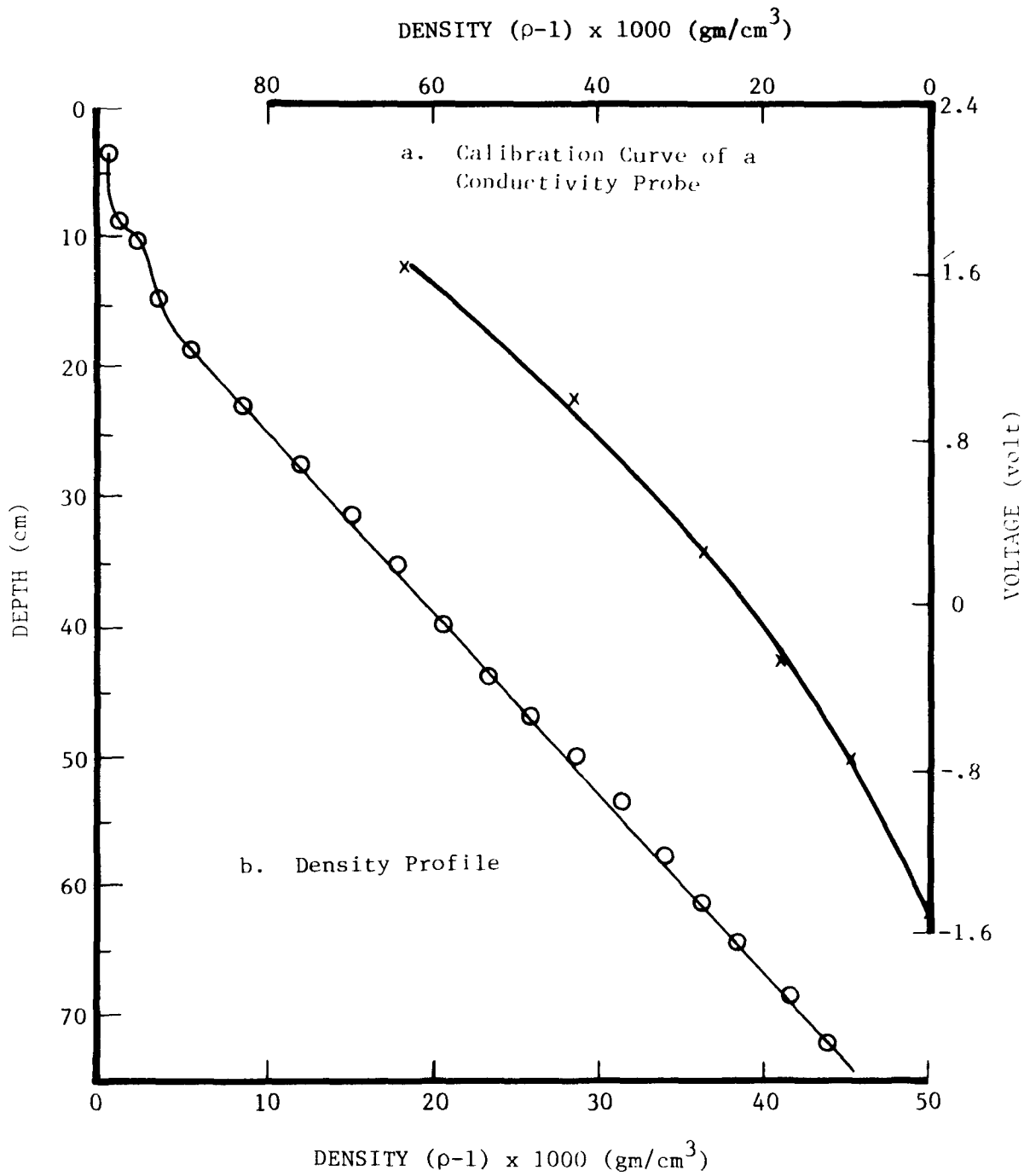
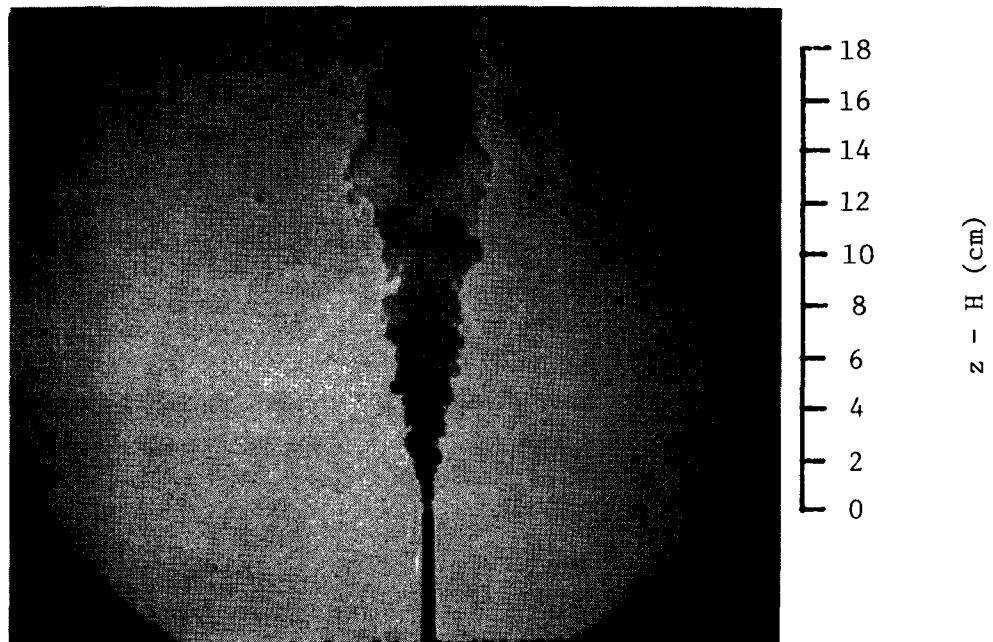
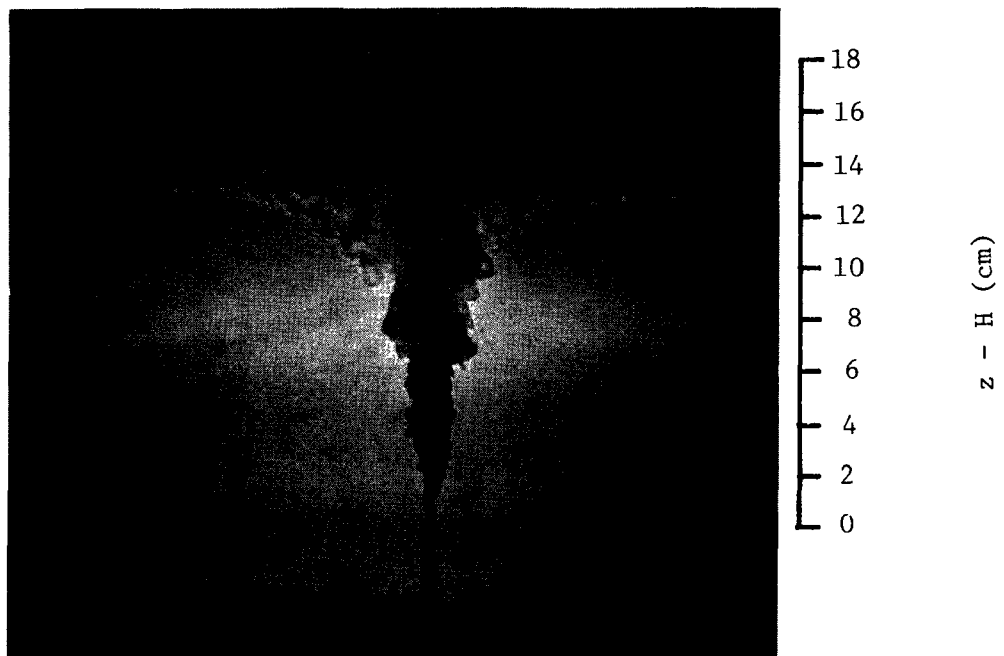


Figure 6. Typical Calibration Curve of a Conductivity Probe and the Density Profile in the Towing Tank



a. Nonstratified Fluid ($N = 0$ Hz)

$$F_D = 2.84$$

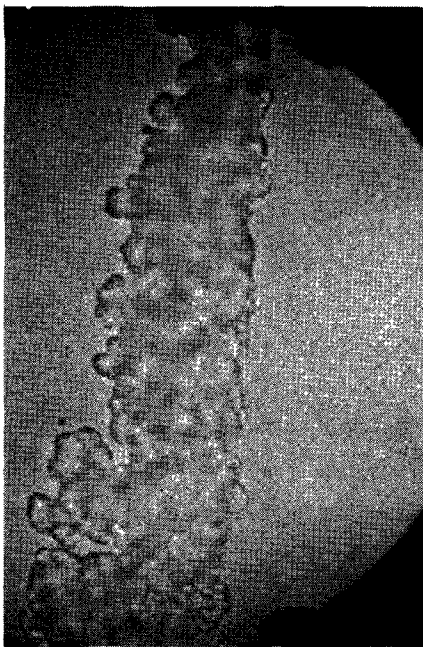


b. Stably Stratified Fluid ($N = .14$ Hz)

$$F_D = 2.92$$

Figure 7. Shadowgraphs of Vertical Plumes in Stagnant Fluids

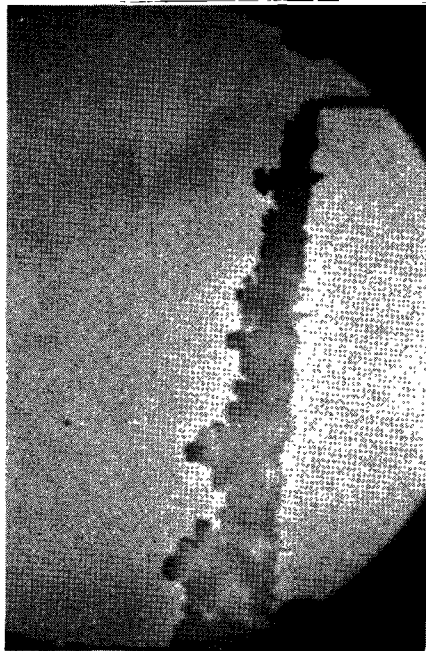
$t = 3 \text{ sec.}$



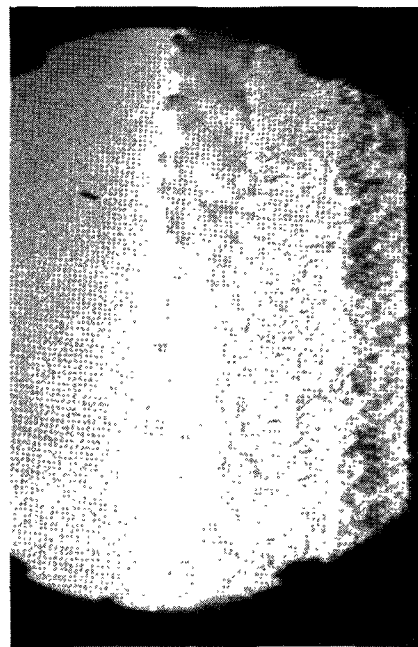
a. Nonstratified Flow $F_H = \infty$, $F_D = 2.84$, $K = 1.7$

10
8
6
4
2
0

z - H (cm)



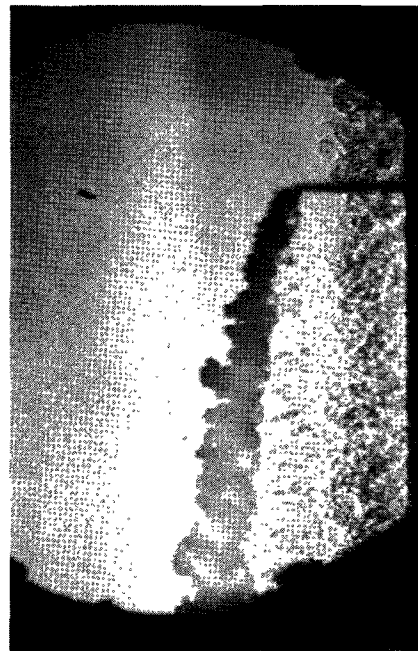
$t = 3 \text{ sec.}$



b. Stably Stratified Flow $F_H = 16.9$, $F_D = 2.92$, $K = 1.7$

10
8
6
4
2
0

z - H (cm)



$t = 0 \text{ sec.}$

Figure 8. Shadowgraphs of Bent-over Plumes in Nonstratified and Stratified Flows

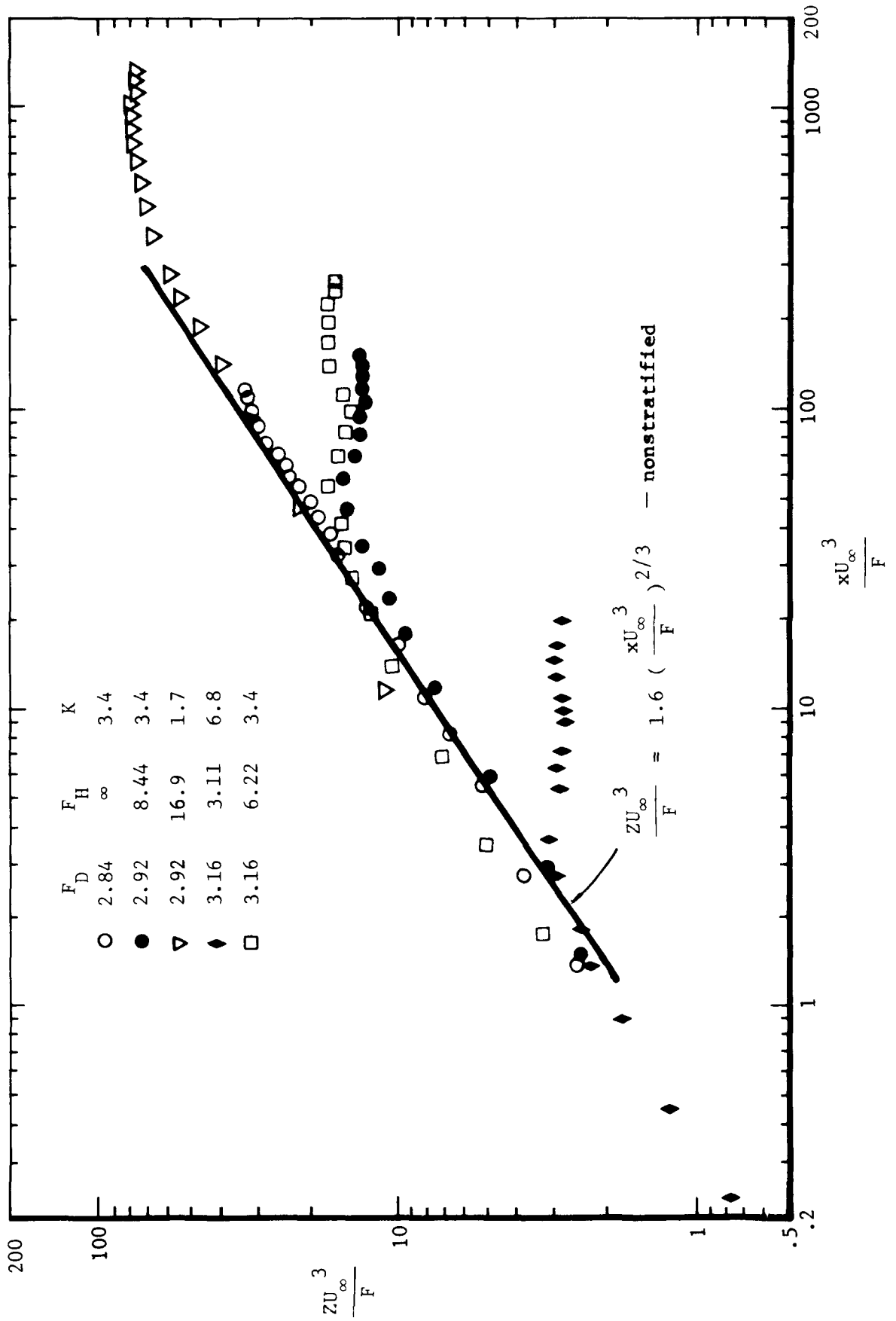


Figure 9. Trajectories of Bent-over Plumes in Nonstratified and Stratified Flows over a Flat Plate

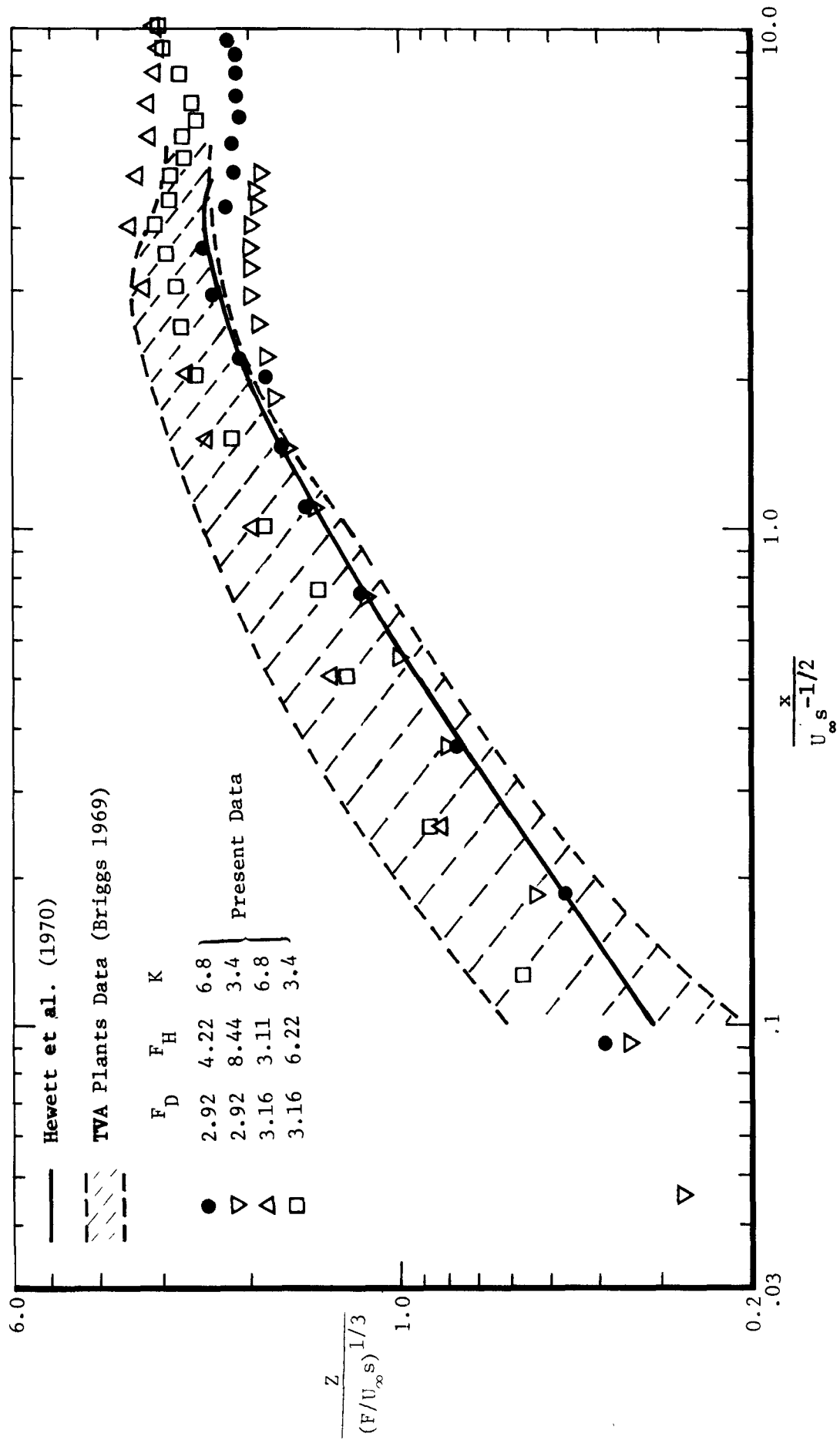


Figure 10. Comparisons of Plume Trajectories in Stratified Fluids among Laboratory and Field Data

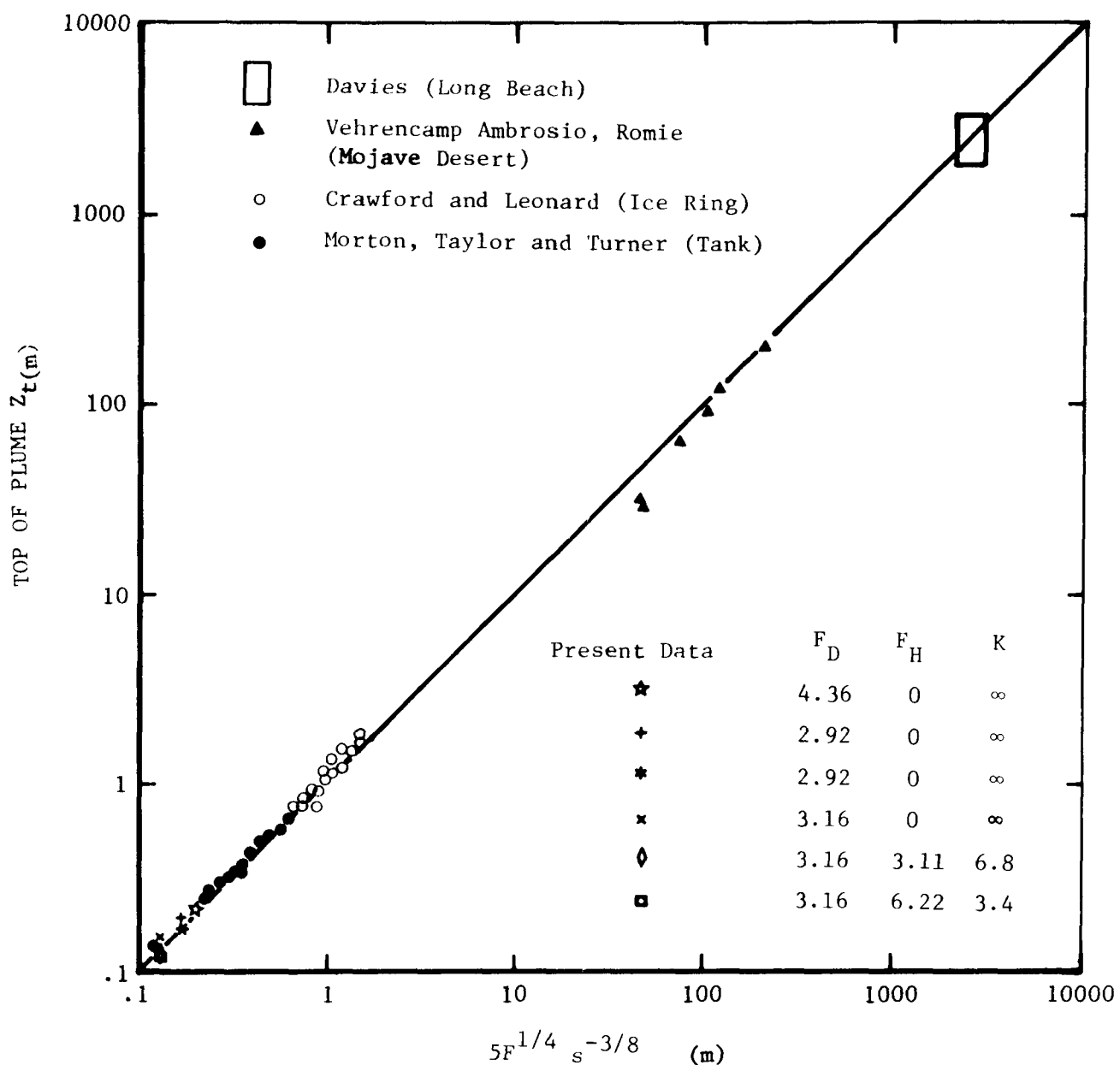


Figure 11. Laboratory and Field Data of Terminal Plume Rises in Calm and Stable Fluids (See Briggs 1969).

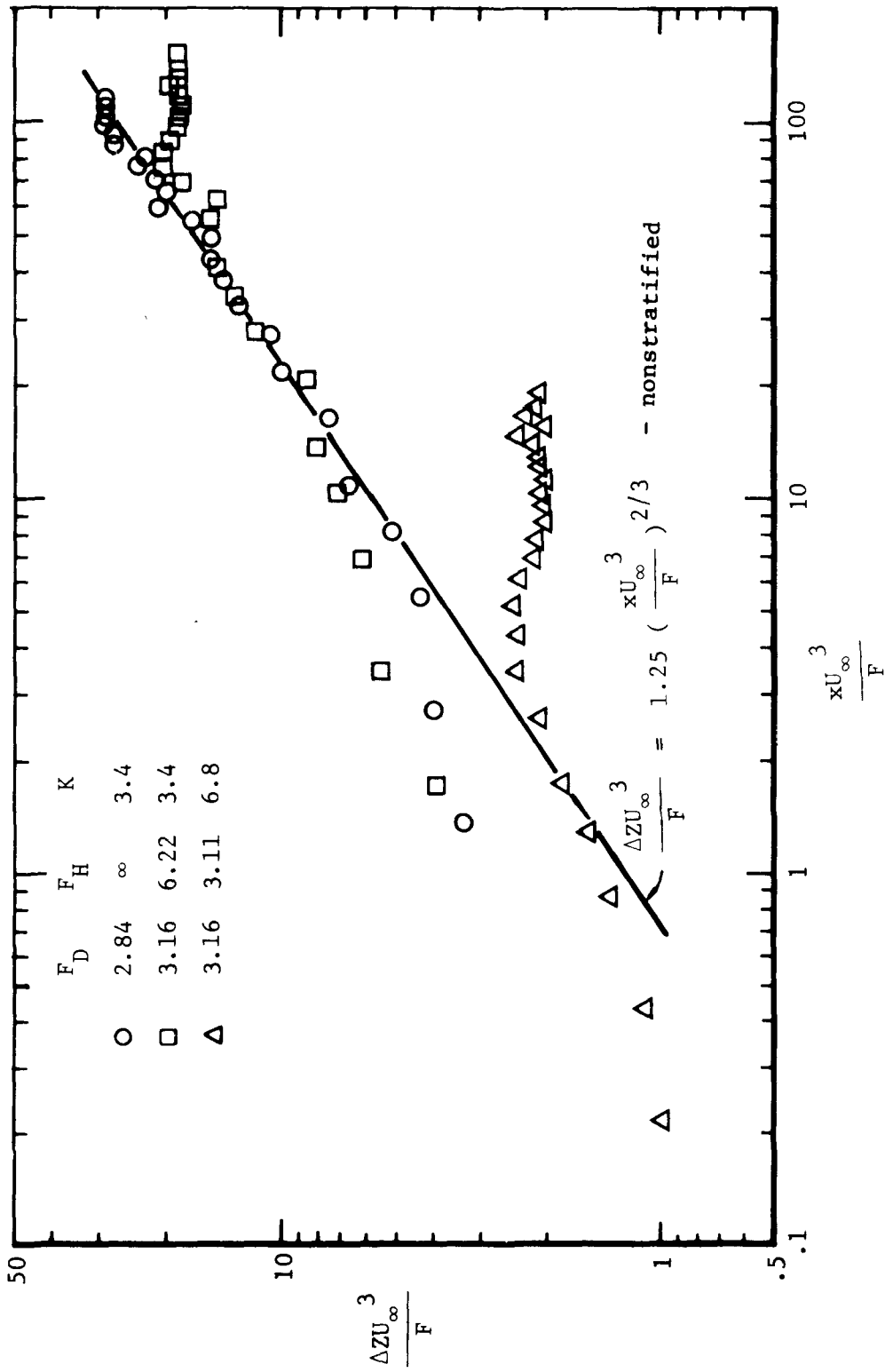


Figure 12. Vertical Spreads of Plumes in Stratified and Nonstratified Flows over a Flat Plate

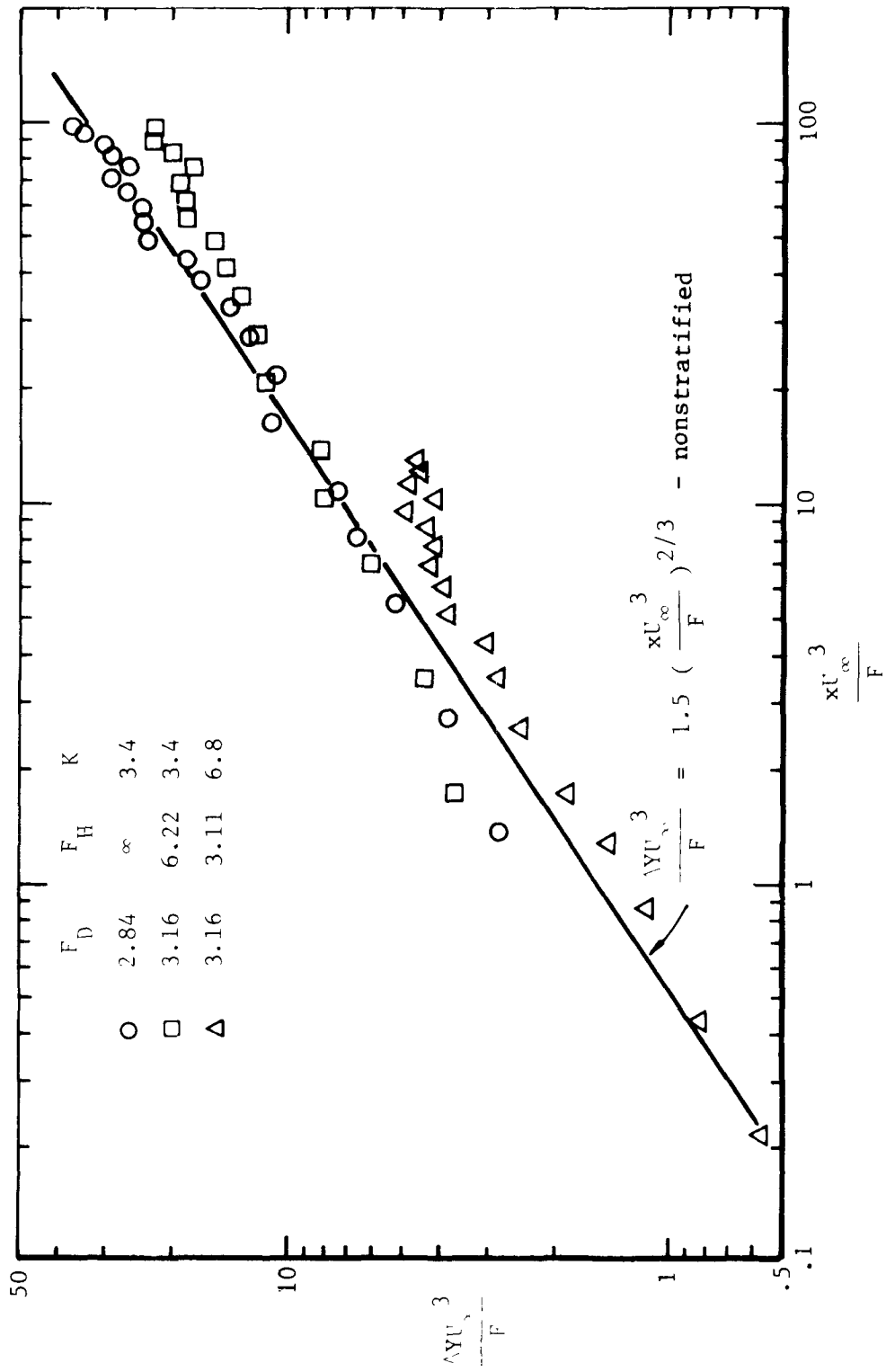
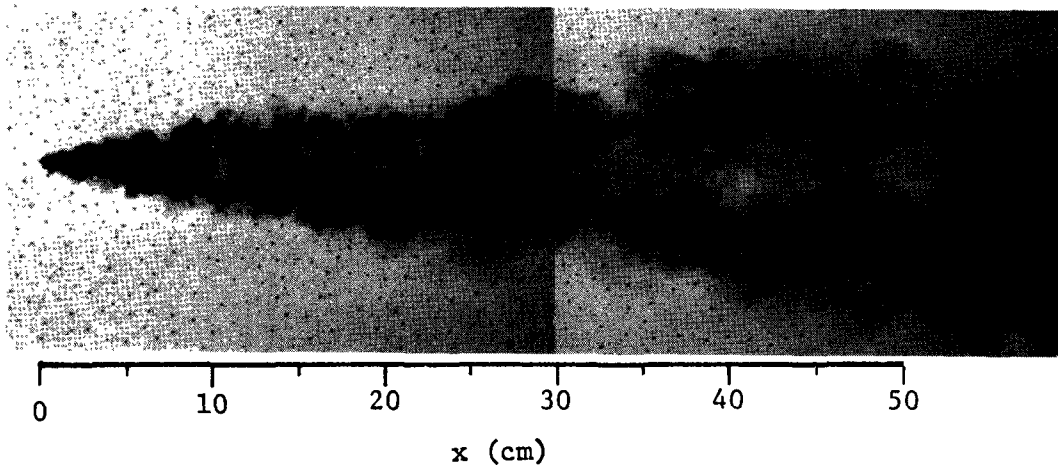
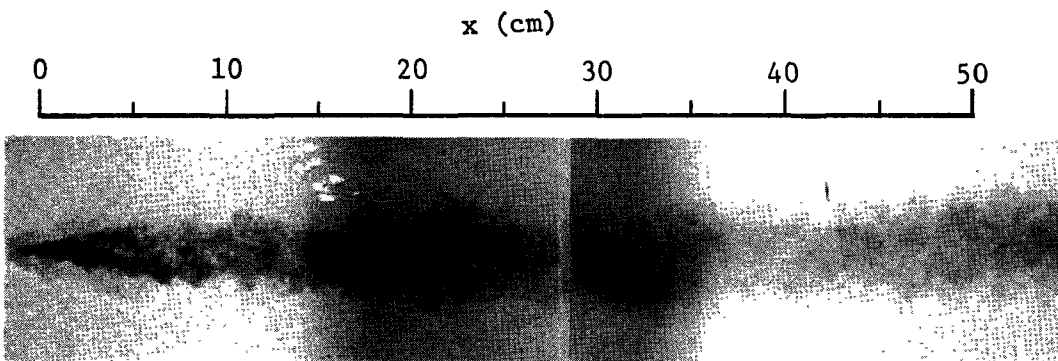


Figure 13. Lateral Spreads of Plumes in Stratified and Nonstratified Flows over a Flat Plate



a. $F_H = \infty$ and $F_D = 2.84$



b. $F_H = 6.22$ and $F_D = 2.92$

Figure 14. The Lateral Spreads of Bent-over Plumes in Nonstratified and Stratified Flows over a Flat Plate. $K = 3.4$ and $R_D = 530$.

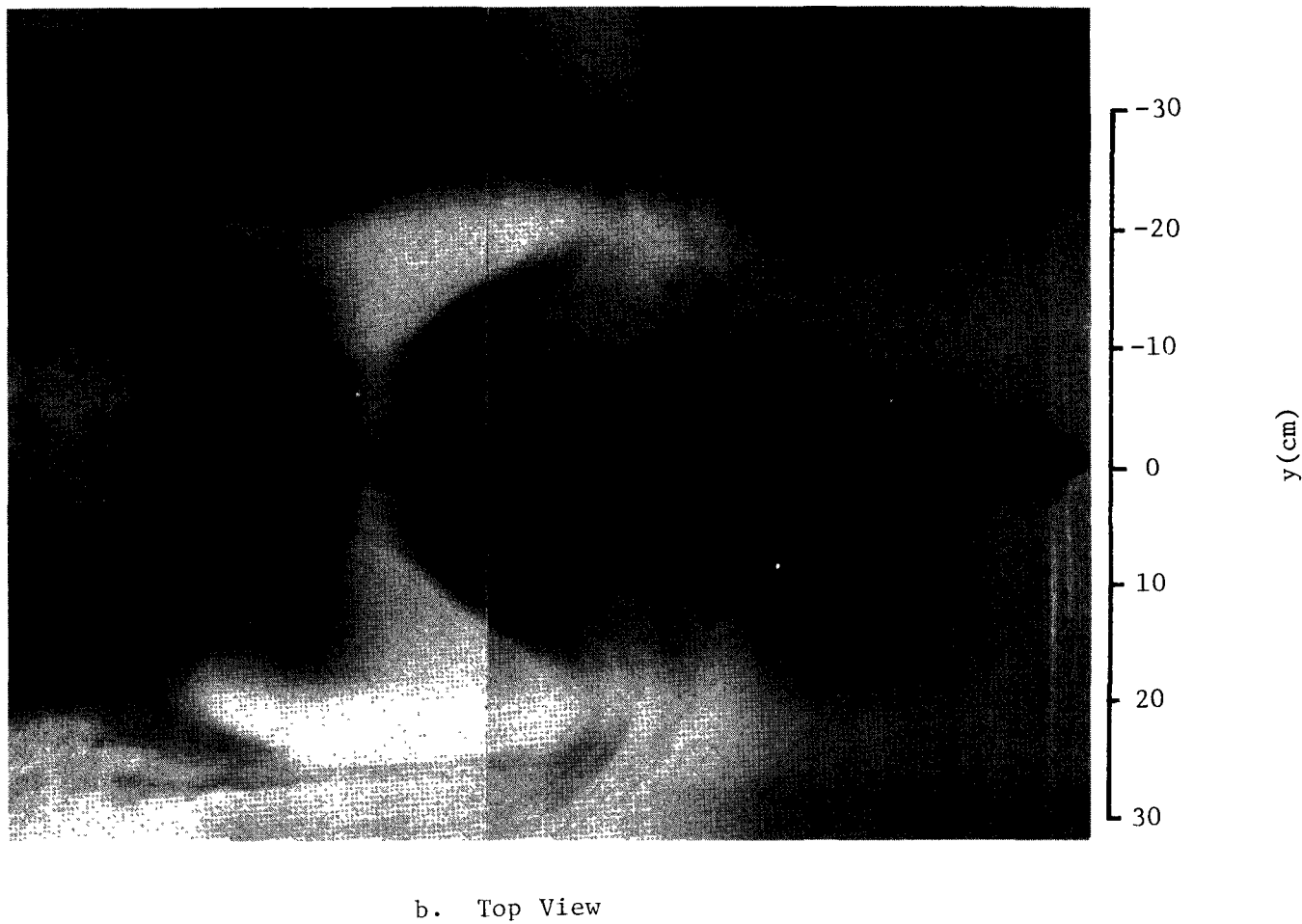
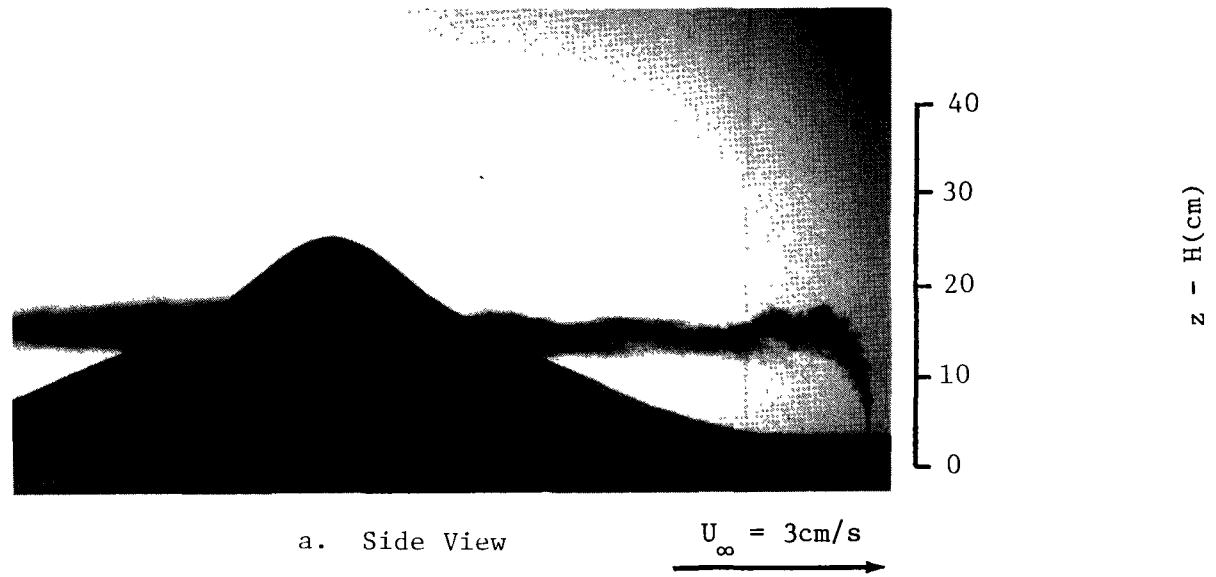


Figure 15. Dye Visualizations of Plume Dispersion in a Stratified Flow over the Terrain Model. $F_D = 3.16$, $F_h = .97$, $K = 6.8$ and $R_D = 530$.

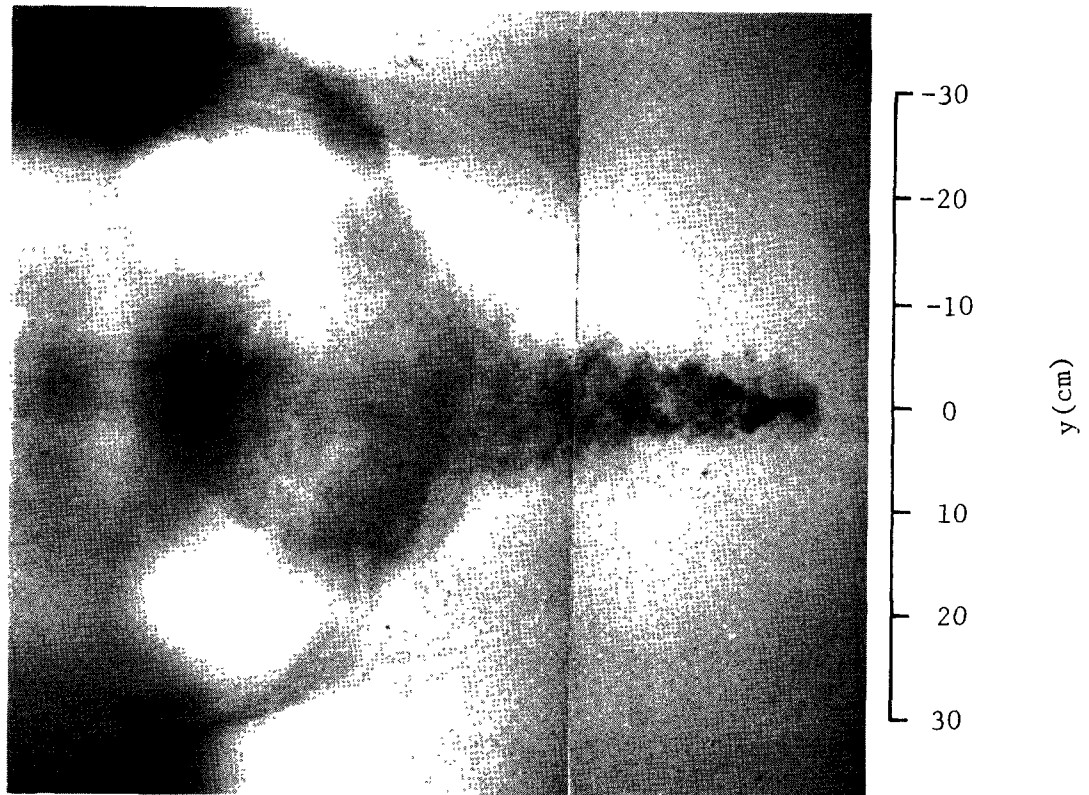
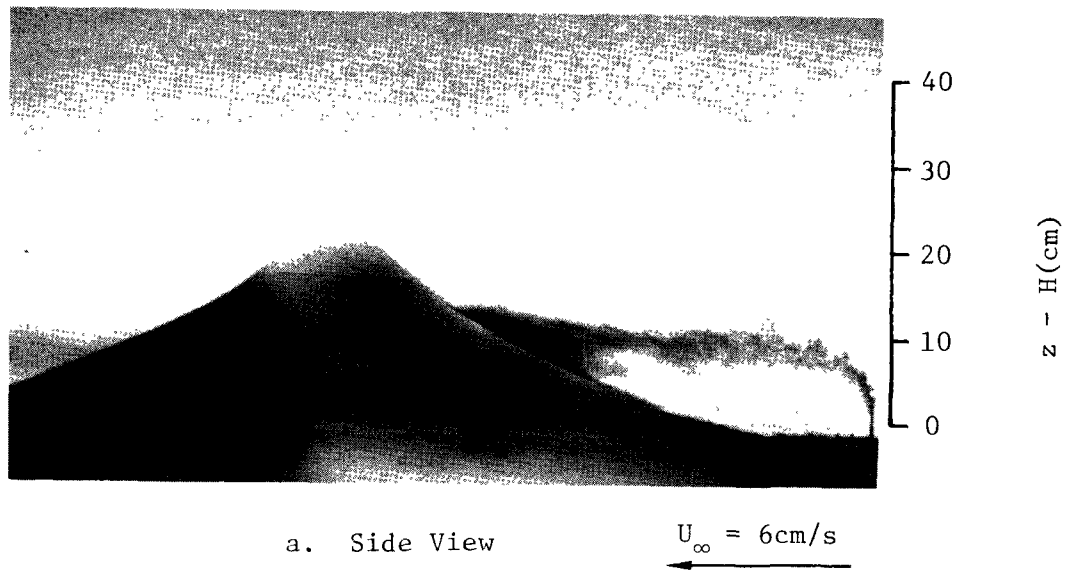
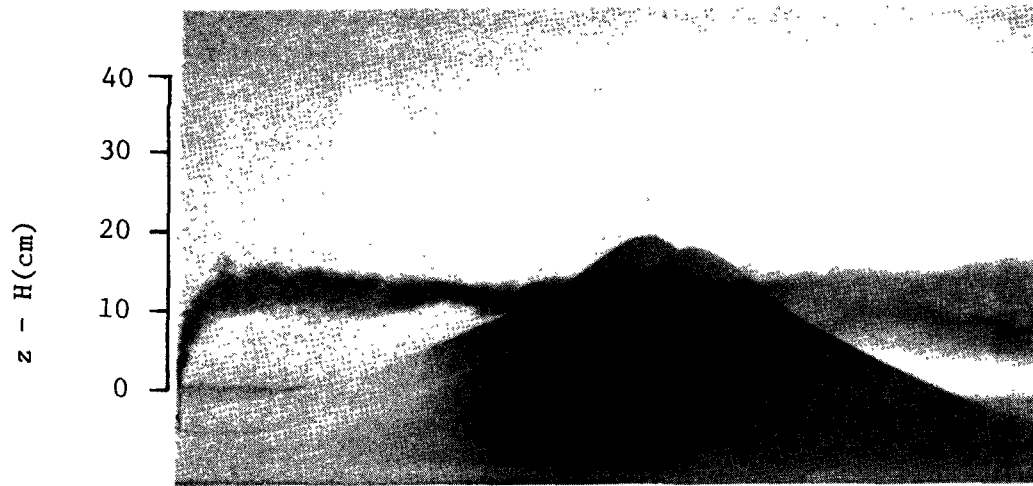

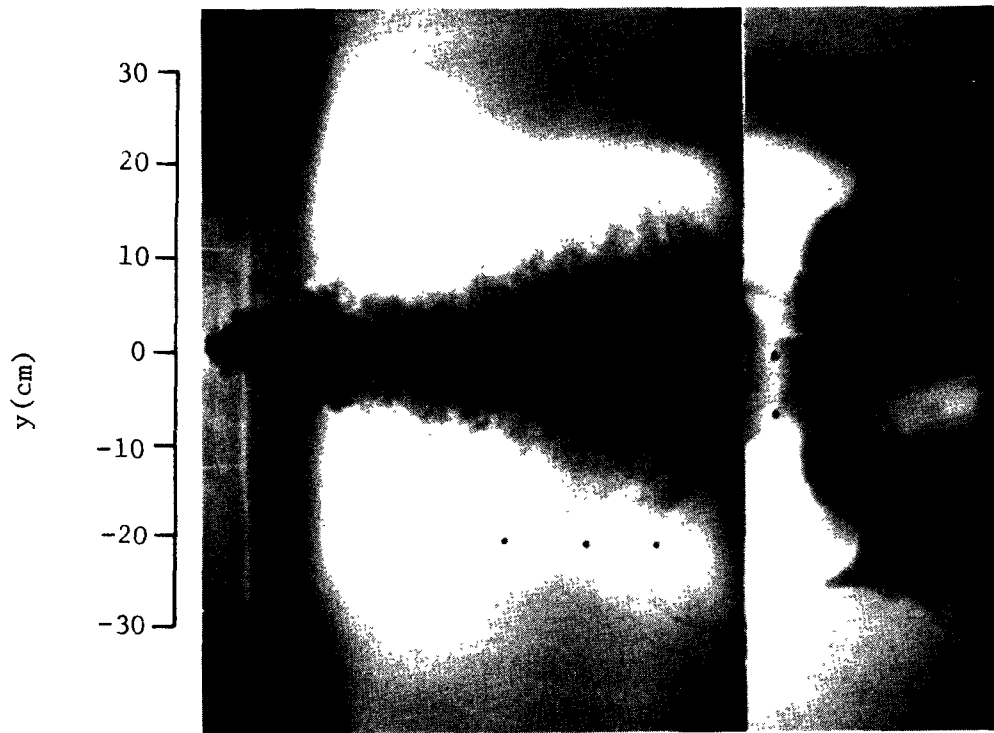


Figure 16. Dye Visualizations of Plume Dispersion in a Stratified Flow over the Terrain Model. $F_D = 3.16$, $F_h = 1.94$, $K = 3.4$, and $R_D = 530$



a. Side View

 $U_{\infty} = 3\text{cm/s}$



b. Top View

Figure 17. Dye Visualizations of Plume Dispersion in a Stratified Flow over the Terrain Model. $F_D = 3.09$, $F_h = 1.32$, $K = 6.8$, and $R_D = 530$.

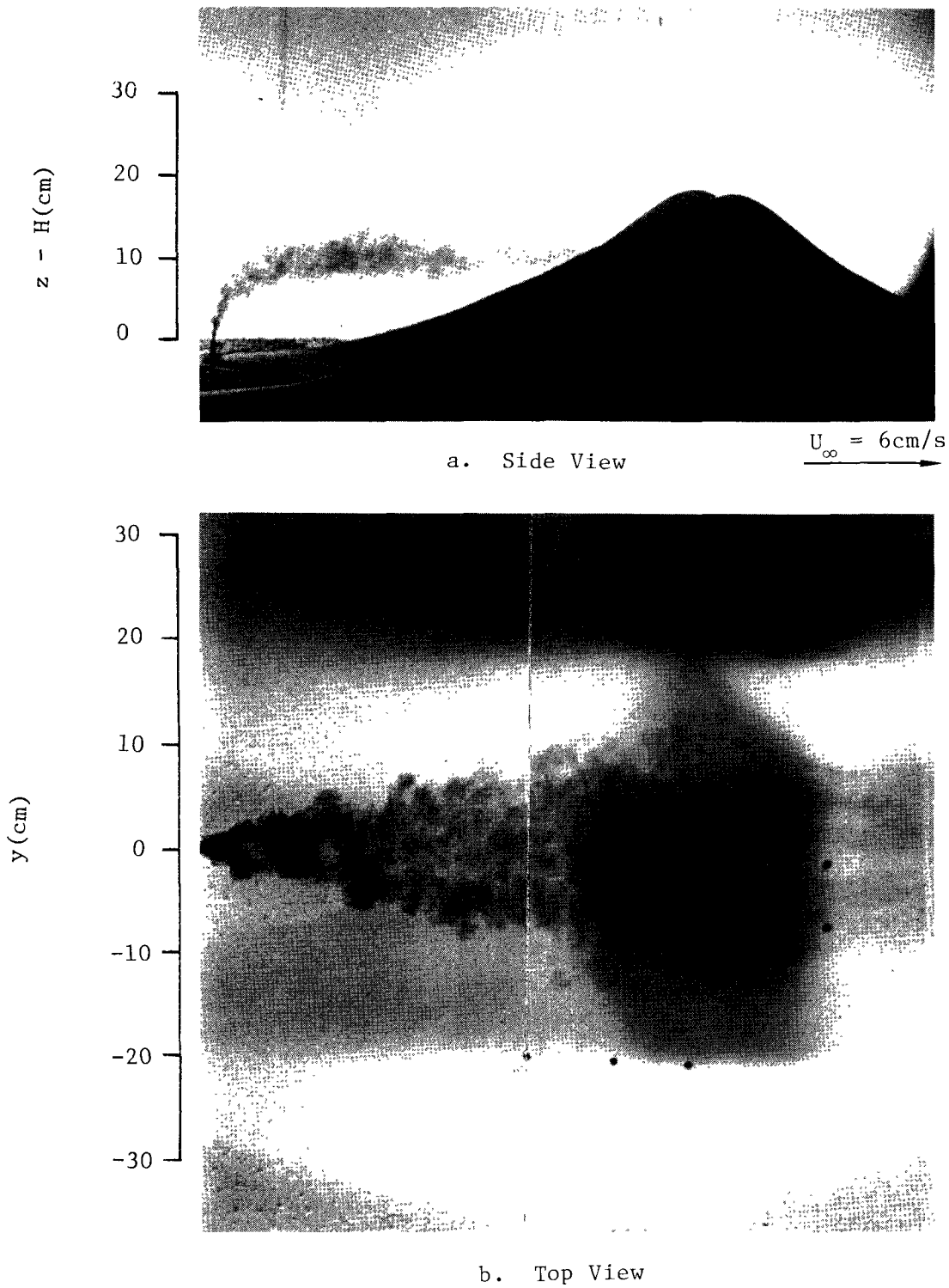


Figure 18. Dye Visualizations of Plume Dispersion in a Stratified Flow over the Terrain Model. $F_D = 3.09$, $F_h = 2.64$, $K = 3.4$, and $R_D = 530$.

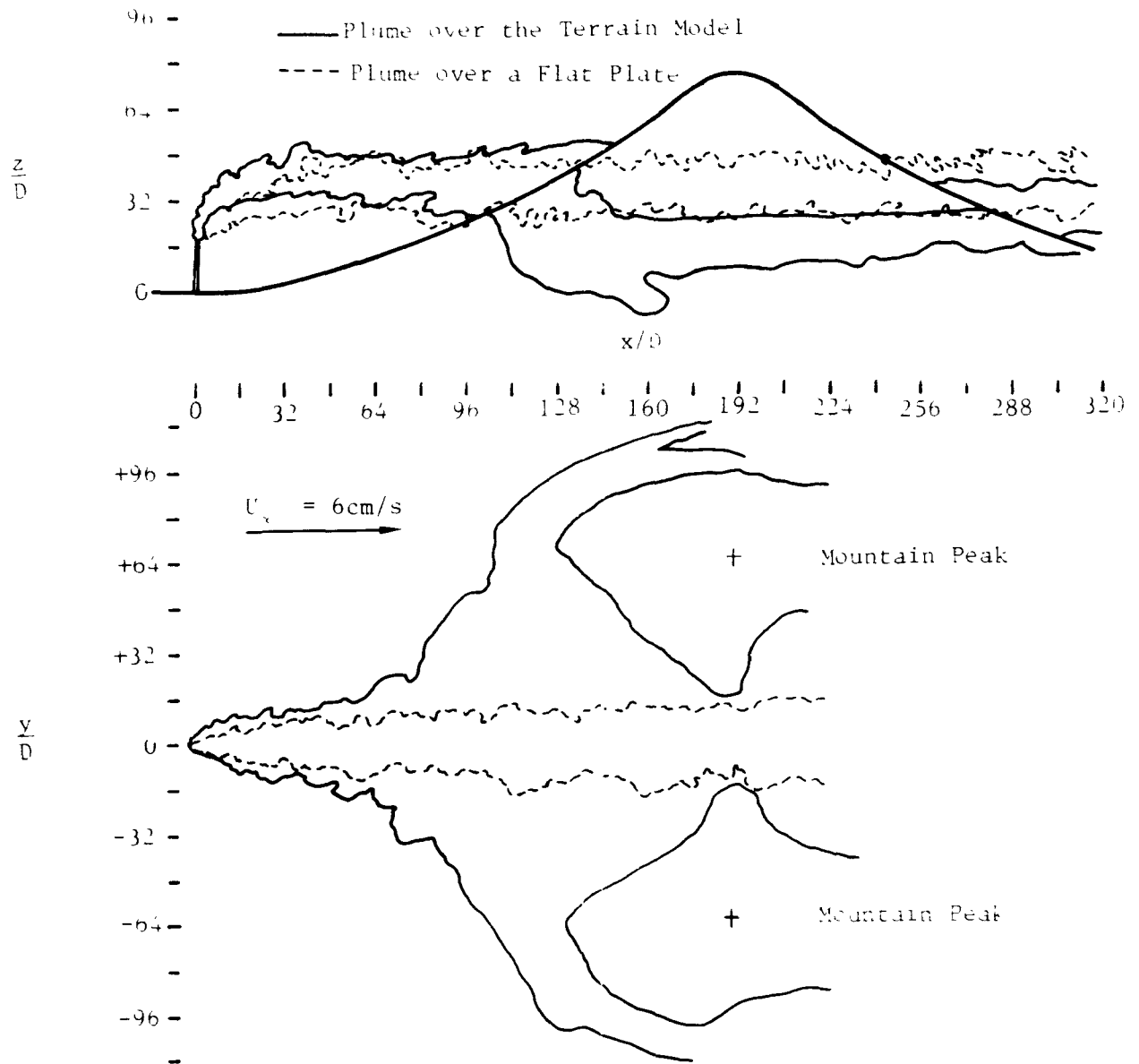


Figure 19. Vertical and Lateral Spreads of Plumes In Stratified Flows over a Flat Plate and the Terrain Model. $F_D = 3.16$, $F_v = 2.64$, $F_H = 6.22$, $K = 3.4$, and $R_D = 530$.

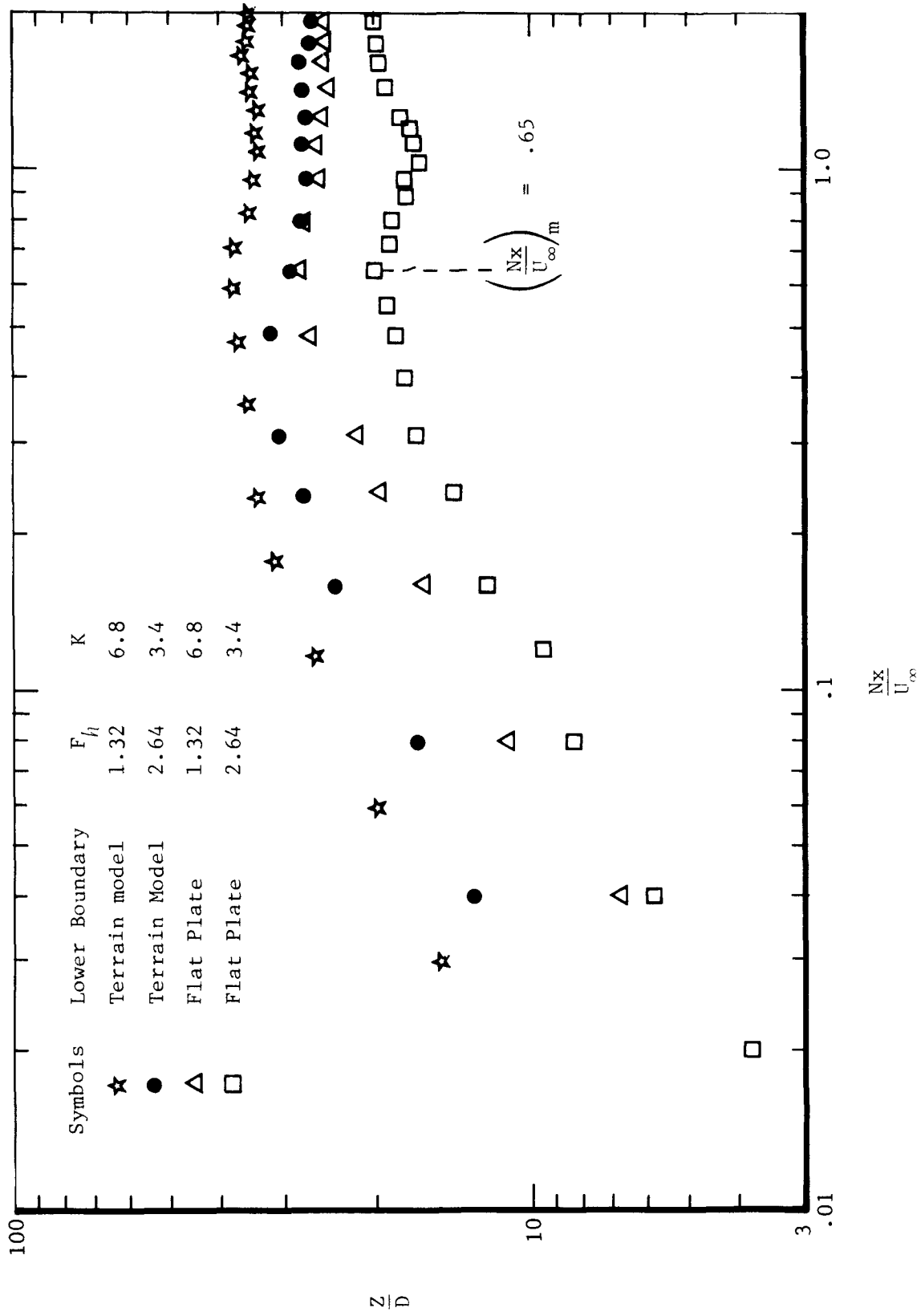


Figure 20. Terrain Effects on the Rise of Plumes ($F_D = 3.16$) in Stably Stratified Flows.

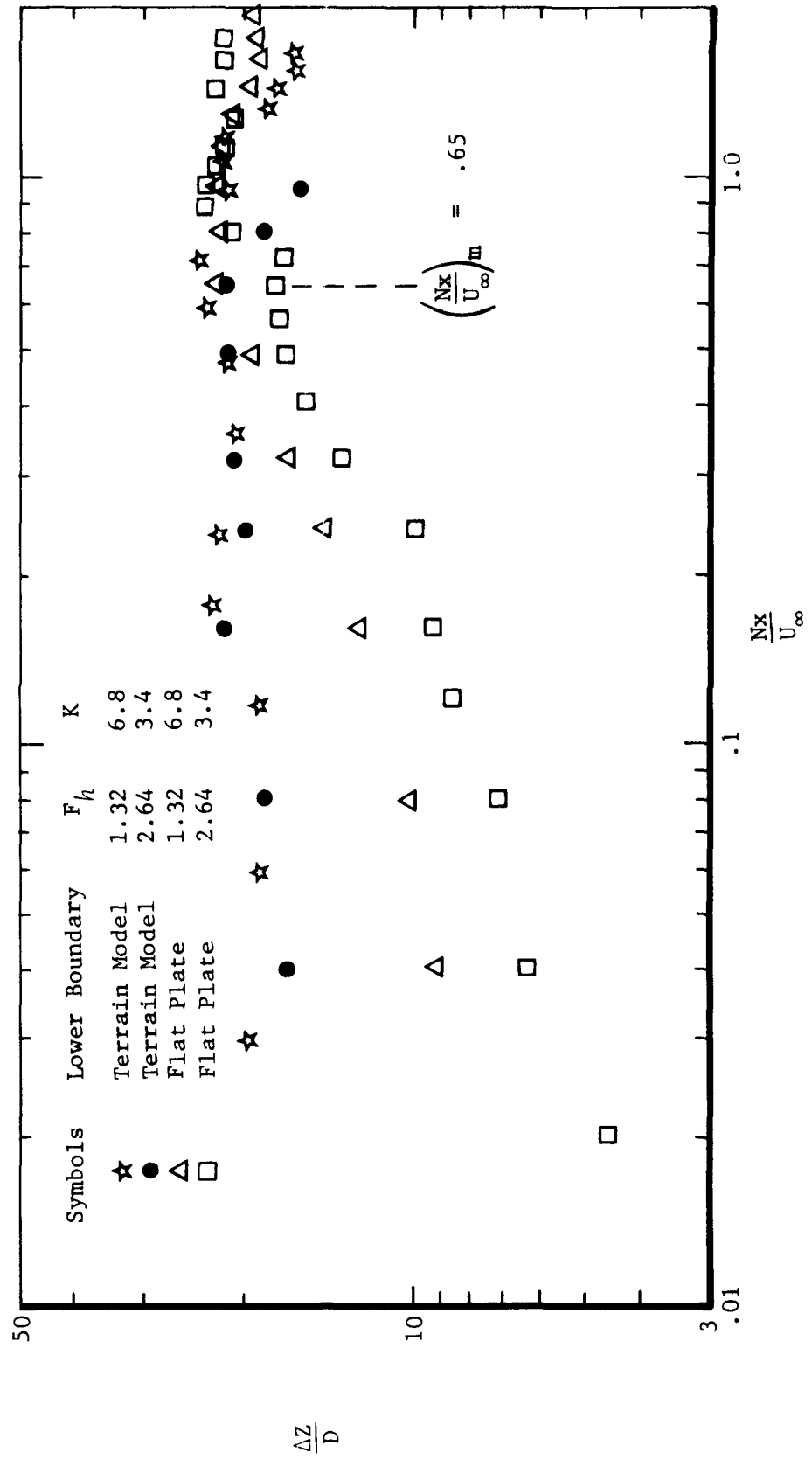


Figure 21. Terrain Effects on the Vertical Spreads of Plumes ($F_D = 3.16$) in Stably Stratified Flows.

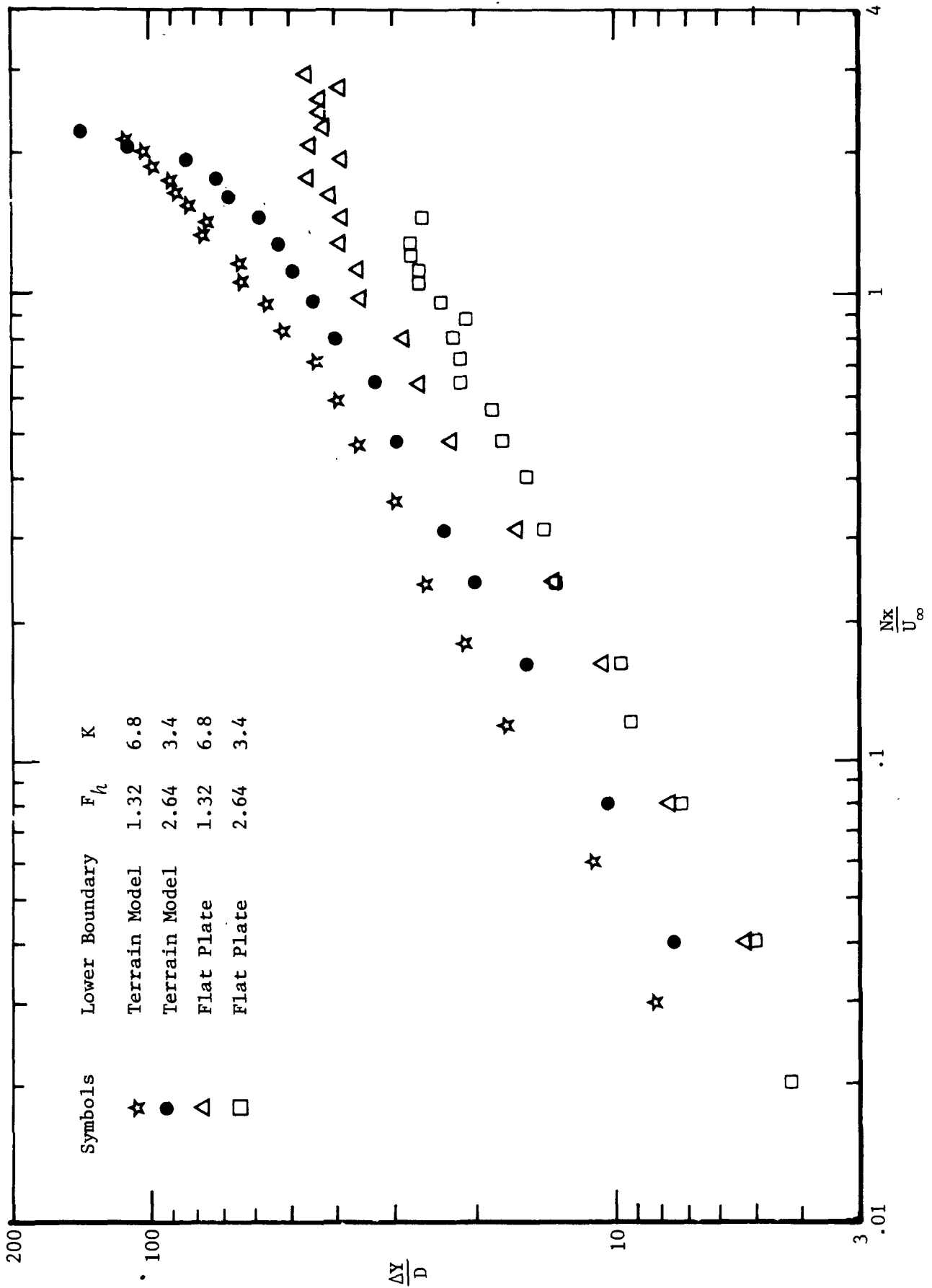
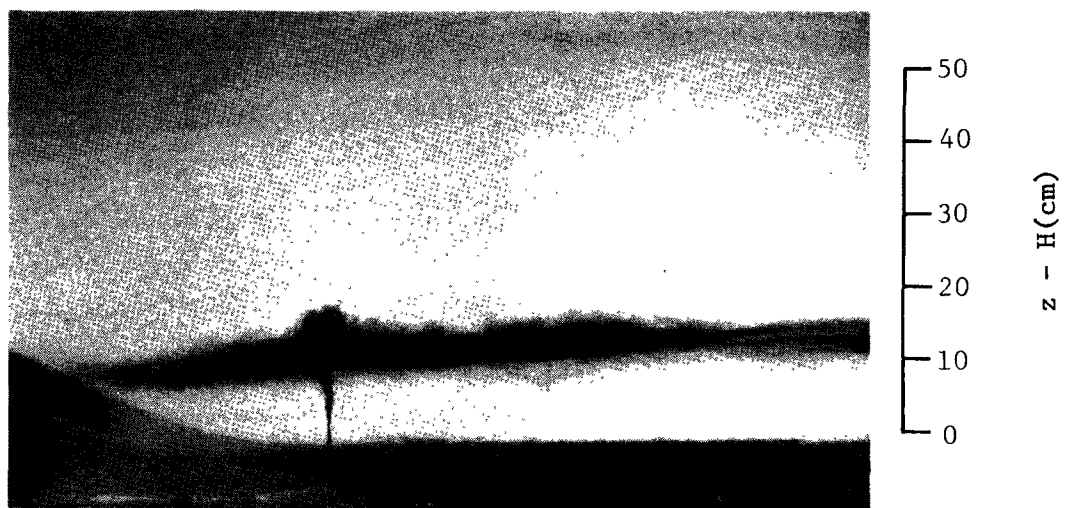
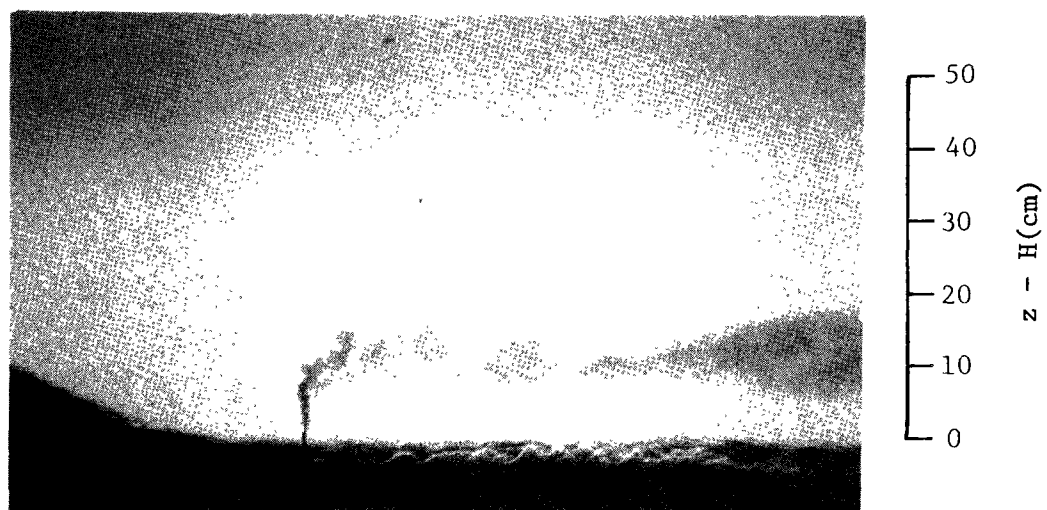


Figure 22. Terrain Effects on the Lateral Spread of Plumes ($F_D = 3.16$) in Stably Stratified Flows.



a. $F_h = 1.32$ $U_\infty = 3\text{cm/s}$ →



b. $F_h = 2.64$ $U_\infty = 6\text{cm/s}$ →

Figure 23. Dye Visualizations of Bent-over Plumes ($F_D = 3.09$) from a Stack Located in the Lee of the Terrain Model.

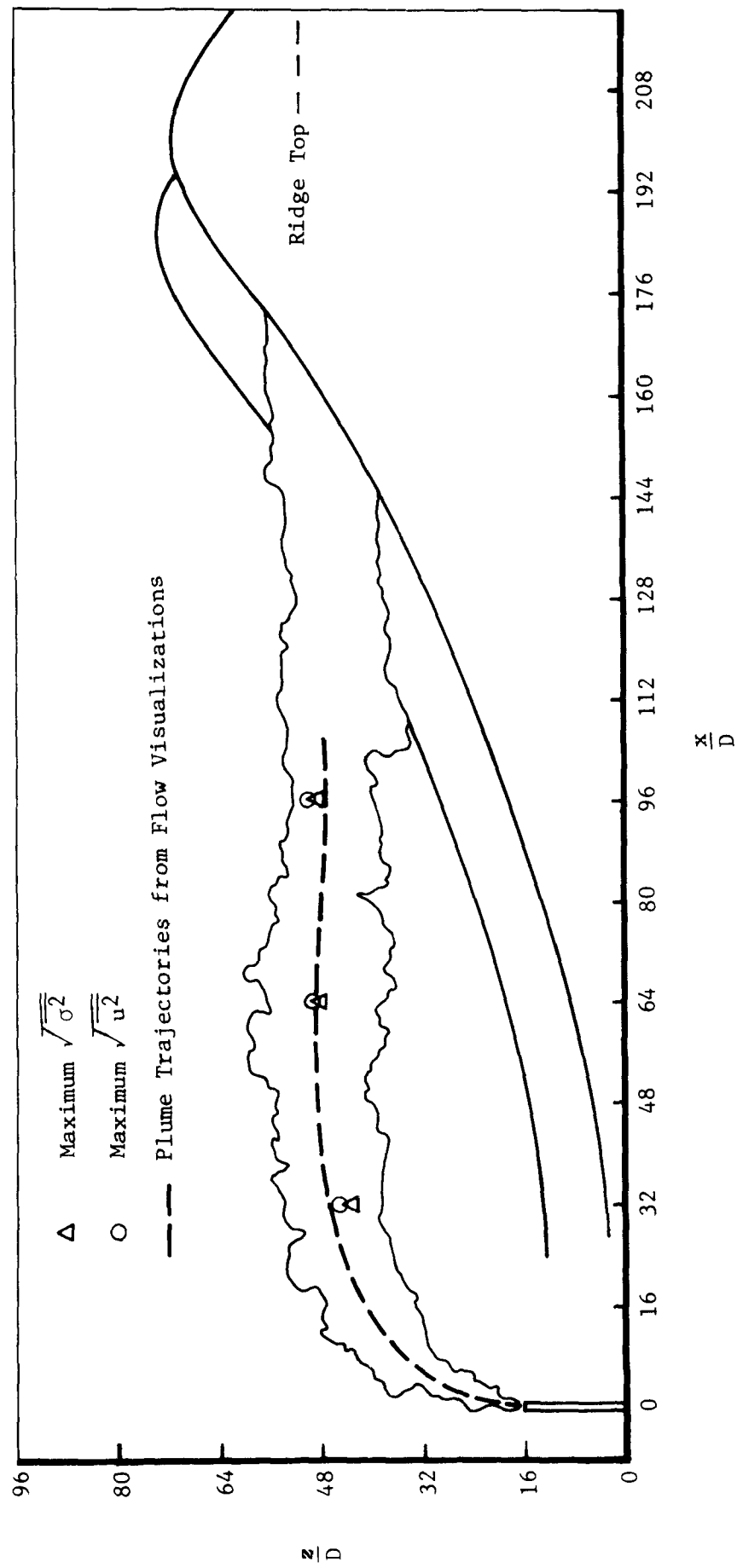


Figure 24. Comparison of Plume Trajectories Determined from Flow Visualizations and from Probe Measurements. $F_D = 3.09$, $F_h = 2.64$, $K = 3.4$, and $R_D = 530$.

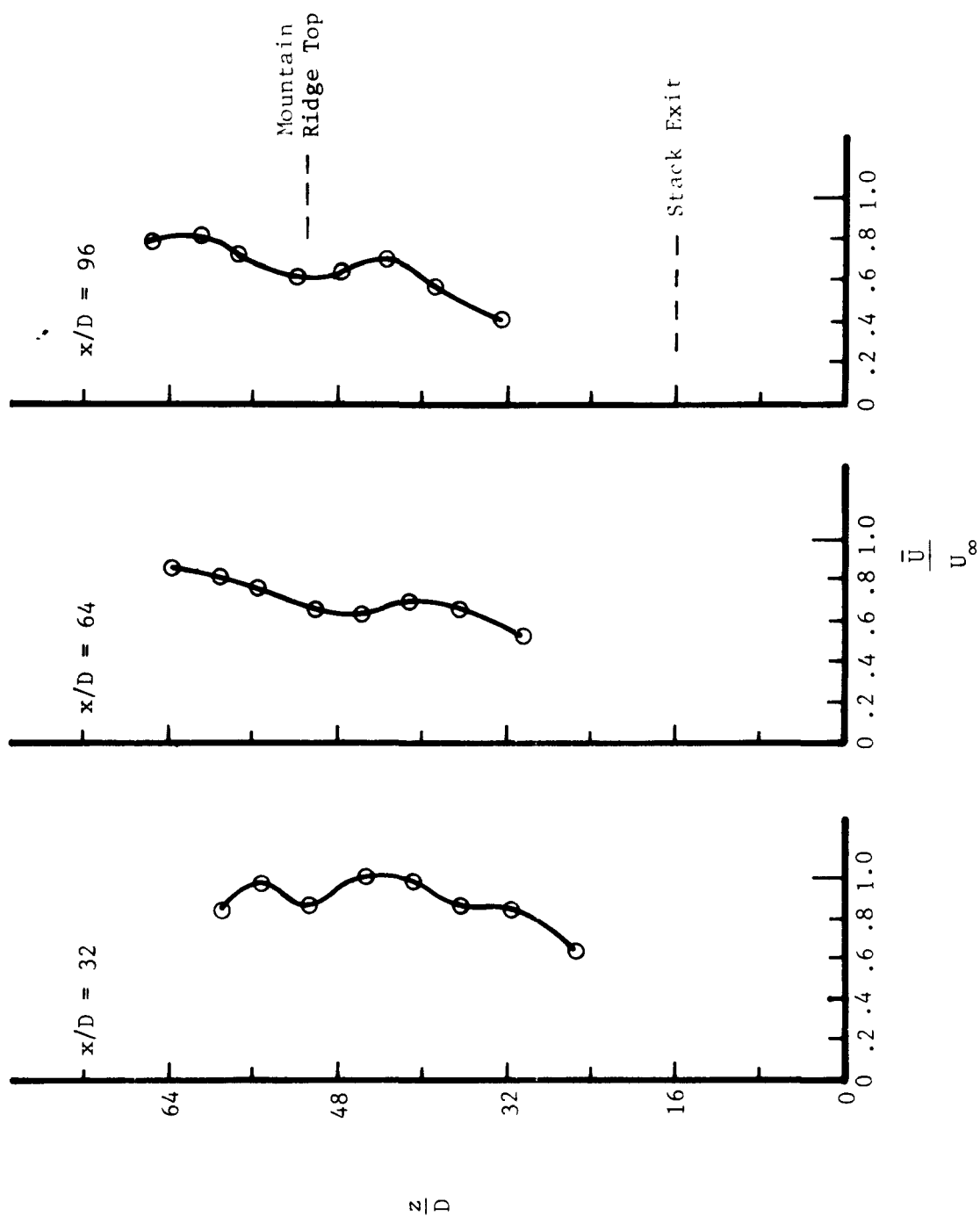


Figure 25. Mean Velocity profiles at Three Stations Upstream of the Terrain Model. $F_1 = 3.09$, $F_{1l} = 2.64$, $K = 3.4$, $R_1 = 530$, and $v/\nu = 3.14$.

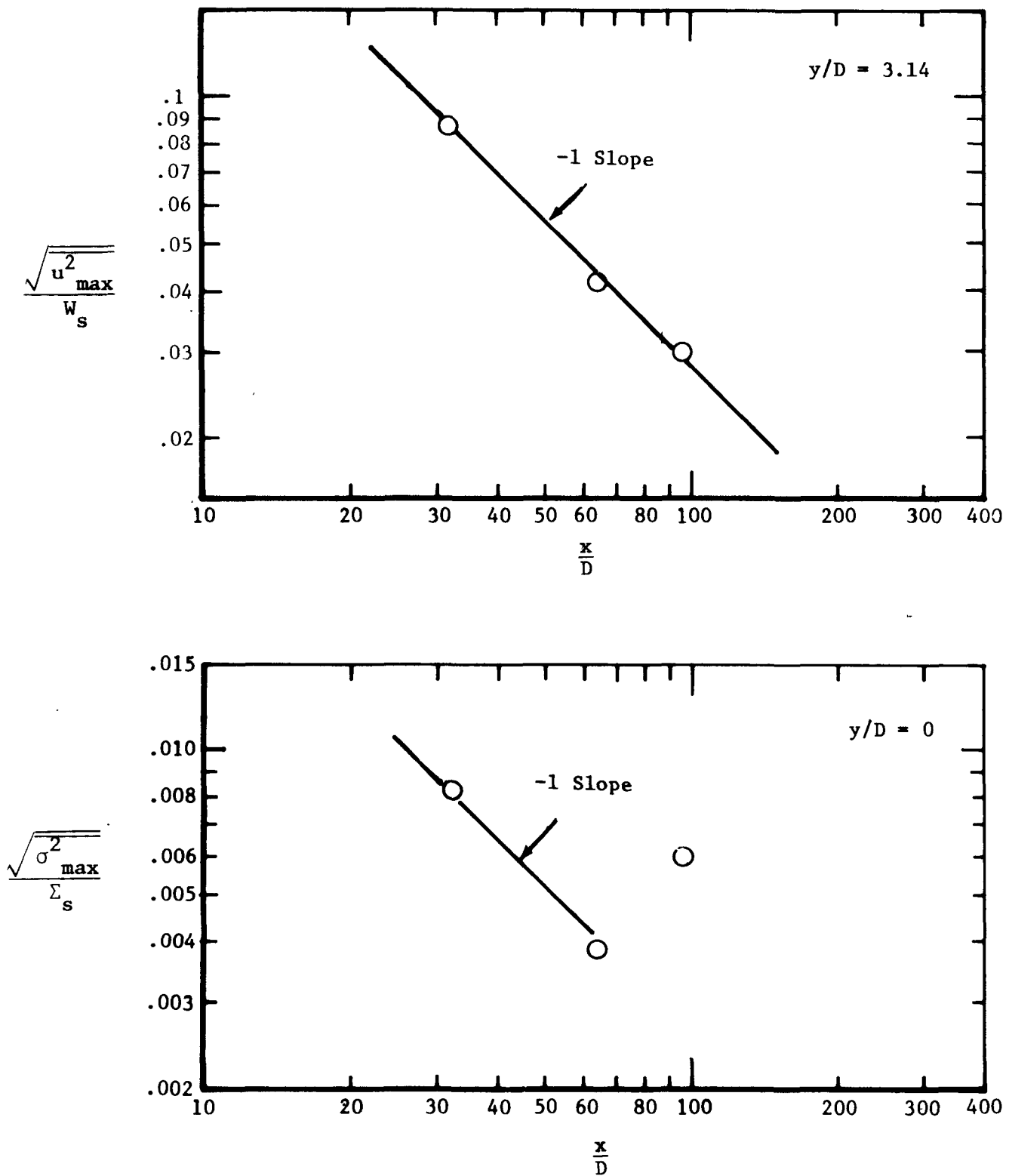
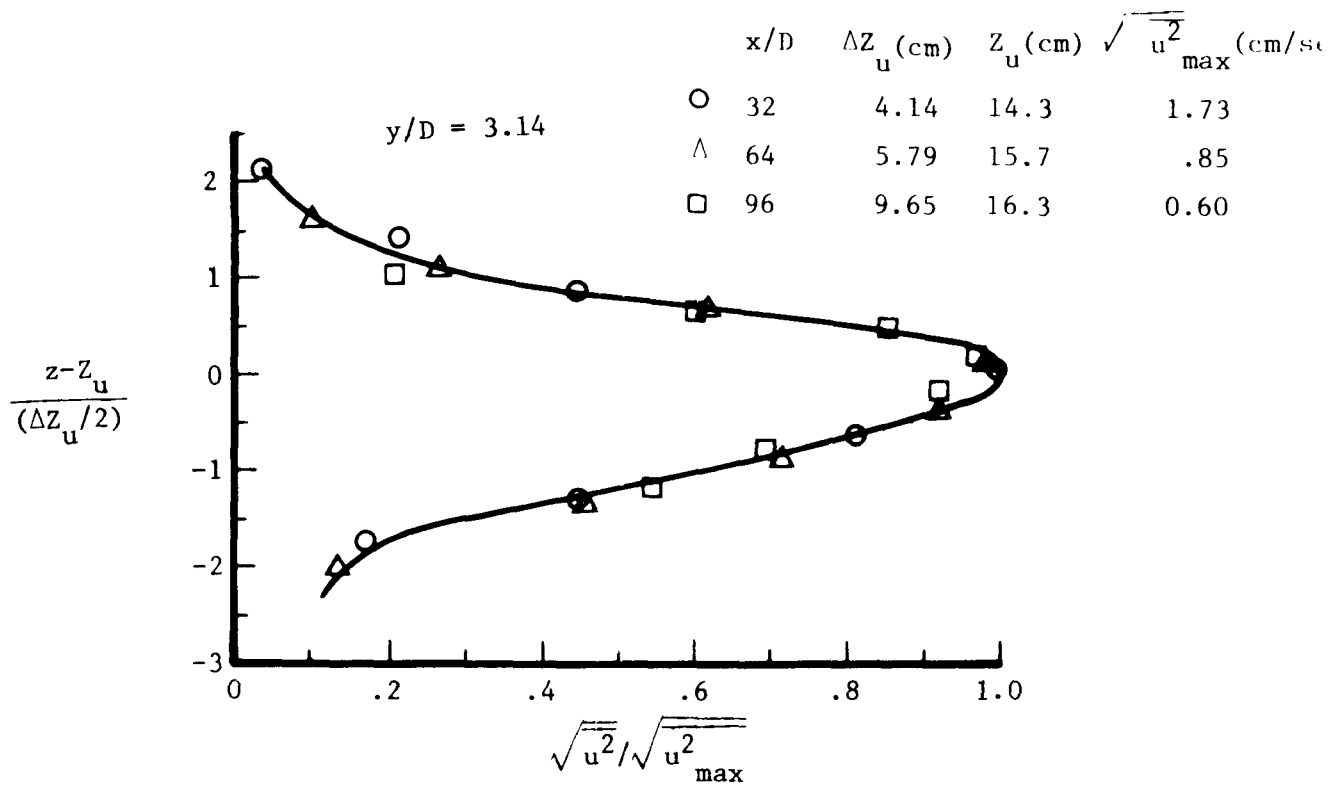
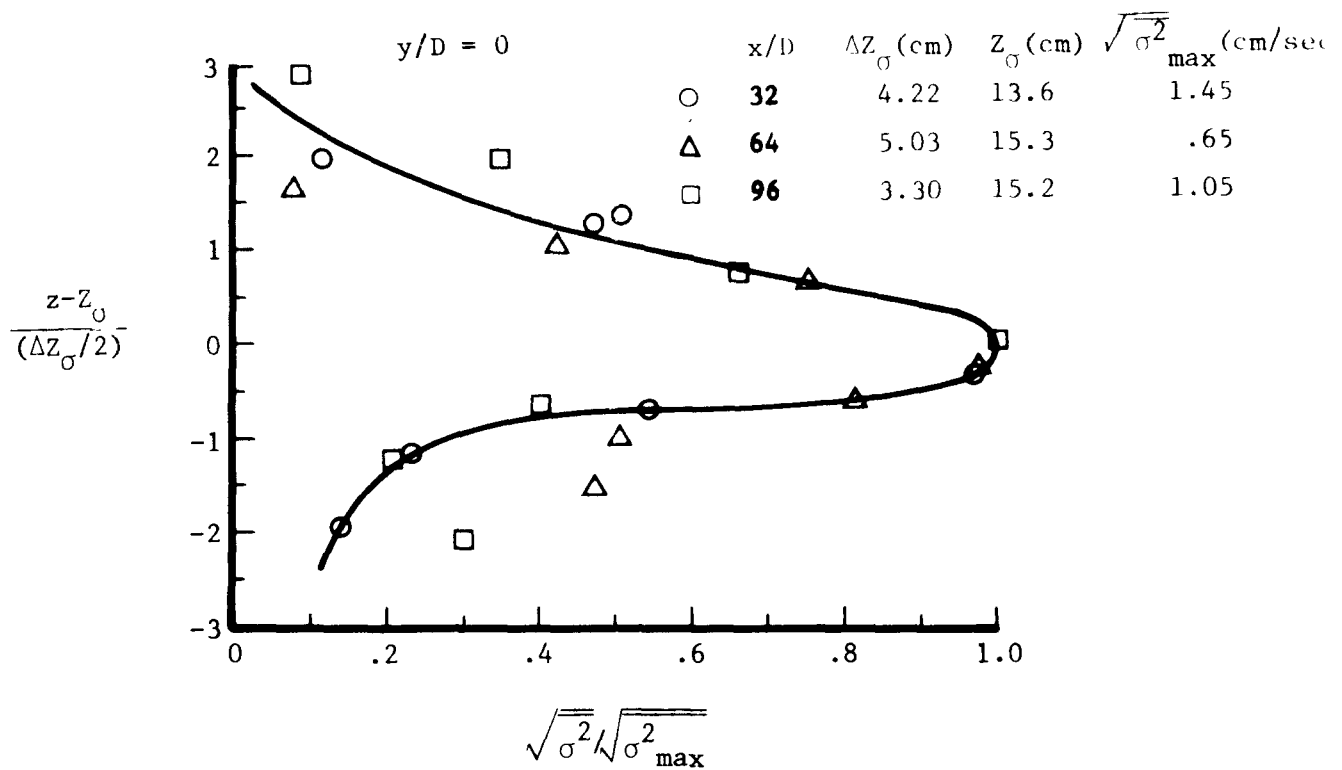


Figure 26. Profiles of Maximum RMS Velocity and Density Fluctuations in the Plume with Downstream Distance from the Stack. $F_D = 3.09$, $F_h = 2.64$, $K = 3.4$, and $R_D = 530$.



a.



b.

Figure 27. Profiles of Normalized RMS Velocity and Density Fluctuations in the Plume. $F_D = 3.09$, $F_h = 2.64$, $K = 3.4$, and $R_D = 530$.

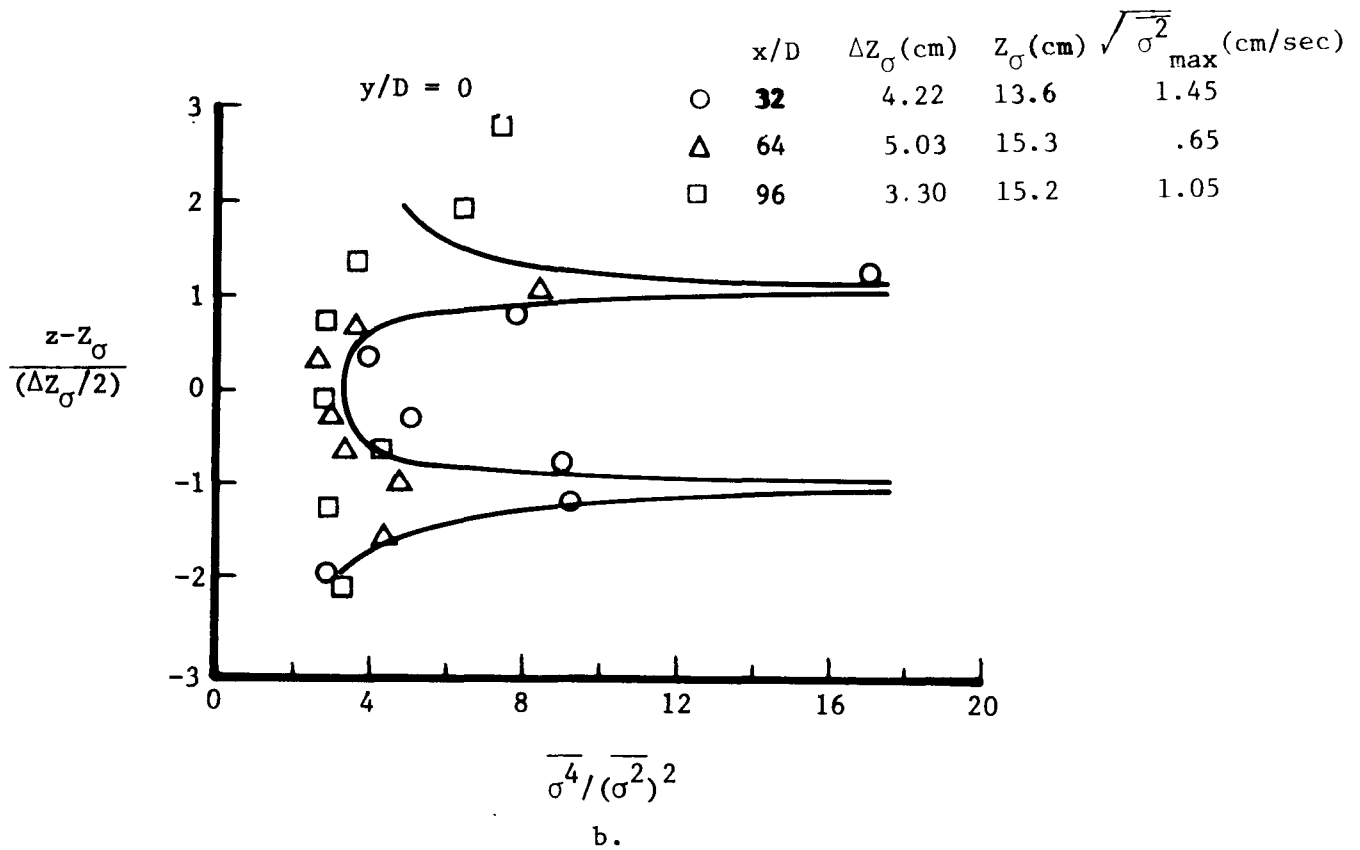
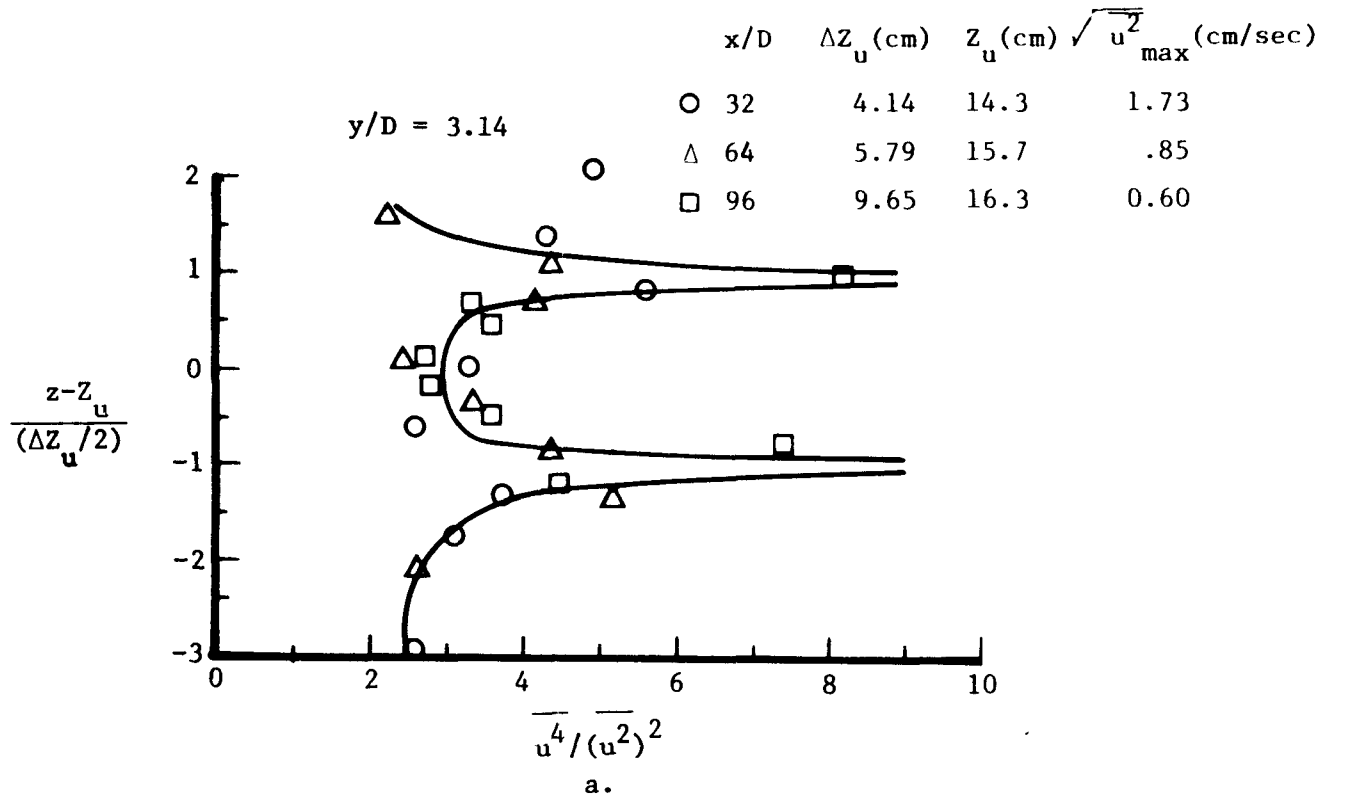


Figure 28. Flatness Factors of Velocity and Density Fluctuations in the Plume. $F_D = 3.09$, $F_h = 2.64$, $K = 3.4$, and $R_D = 530$.

TASK II

A FEASIBILITY STUDY OF NUMERICAL SIMULATION
OF PLUME DISPERSION IN STABLY STRATIFIED
FLOWS OVER A COMPLEX TERRAIN

A Feasibility Study of Numerical Simulation of Plume
Dispersion in Stably Stratified Flows over Complex Terrain

by

Flow Research, Inc., Kent, Washington 98031

I. Introduction

Flow Research, Inc. has considered several alternative approaches to the numerical modelling of realistic flow fields with simple source diffusion in the vicinity of complex terrain. Our approach to this problem has followed several diverse paths, all of which we believe add to give a comprehensive modelling approach that is most appropriate to guide future work.

In Part A (Flow Research Note No. 40, "Calculation of Stably Stratified Flow Around Complex Terrain" by D. K. Lilly), a method is proposed for the calculation of strongly stratified flow in complex terrain. This method is expected to be useful for modelling single source diffusion of pollutants when the source lies below the mountain tops. Extensions of this model are proposed to handle the effects of a turbulent atmospheric boundary layer, as well as mountain lee waves.

The method proposed in Note No. 40 involves a Froude number expansion of the steady state Boussinesq equations of motion. The Froude number ϵ is defined by

$$\epsilon = U^2 / h^2 N^2$$

where h is the mountain height, U is a characteristic horizontal velocity, and $N^2 = -\frac{g}{\rho_0} \frac{\partial \rho}{\partial z}$ is the square of the Brunt-Vaisala frequency. If the potential energy required to lift fluid to the mountain top is much larger than the kinetic energy of the fluid then ϵ is very small. It seems that in cases of strong stratification, it suffices to truncate the Froude number expansion at first order. This expansion technique applies directly to the flow field. Using K-theory and the resulting flow field, it is then possible to calculate the single source diffusion of a pollutant in this strongly stratified environment. This method will be explored further under the current EPA Contract No. 68-02-1293.

We have also studied the feasibility of performing spectral computations in complex terrains. A brief description of a possible technique for doing this follows. Suppose the terrain is given by $z = f(x, y)$, where z is the vertical height of the ground. We suppose that the top of the computational domain is $z = z_T$ independent of x, y (for simplicity). We then introduce new coordinates

$$\begin{aligned} x' &= x \\ y' &= y \\ z' &= 1 - \frac{z_T - z}{z_T - f(x, y)} \end{aligned}$$

so that $0 \leq z' \leq 1$. In terms of these coordinates, derivatives are transformed into

$$\frac{\partial F(x, y, z)}{\partial x} = \frac{\partial F}{\partial x'} - (1 - z') \frac{\frac{\partial f(x', y')}{\partial x'}}{z_T - f(x', y')} \frac{\partial F}{\partial z'}$$

$$\frac{\partial F(x, y, z)}{\partial y} = \frac{\partial F}{\partial y'} - (1 - z') \frac{\frac{\partial f(x', y')}{\partial y'}}{z_T - f(x', y')} \frac{\partial F}{\partial z'}$$

$$\frac{\partial F(x, y, z)}{\partial z} = \frac{z_T}{z_T - f(x', y')} \frac{\partial F}{\partial z'}$$

Since the functions

$$\frac{\frac{\partial f}{\partial x}}{z_T - f}, \frac{\frac{\partial f}{\partial y}}{z_T - f} \quad \text{and} \quad \frac{z_T}{z_T - f}$$

can be easily stored a priori in their spectral forms, it follows that evaluation of derivatives, nonlinear terms, etc., can be easily implemented using the techniques already extensively developed by Orszag and others.

Spectral simulations of the type discussed here, when applied to the Boussinesq time-dependent equations of motion, have several advantages over finite-difference simulations of the same flows, especially the absence of phase errors in the propagation of linear theory waves. These advantages

appear whether or not $f(x,y)$ is smoothly continuous, but they are more obviously realized when $f(x,y)$ is smooth. Such spectral simulations have the advantage over the Froude number expansion discussed above of applying in both stable and unstable environments. In addition, the effects of atmospheric turbulence can be explicitly taken into account by means of turbulence transport models or sub-grid scale nonlinear eddy viscosity coefficients. These full spectral simulations together with associated single source diffusion calculations can provide a complete set of atmospheric data for the evaluation of environmental impact of proposed installations.

Flow Research, Inc. has also made a careful study of techniques for the imposition of radiation boundary conditions in numerical calculations. In Part B (Flow Research Report No. 30, "Numerical Simulation of Radiation Boundary Conditions" by M. Israeli and S. A. Orszag), several methods are discussed for the imposition of radiation conditions. This problem is particularly important in the stratified atmospheric environment in several respects. First, numerical models of atmospheric motions are generally performed with some kind of lid affixed to the top of the atmosphere. If this lid reflects internal waves back into the computational domain, the computations can be degraded and serious inaccuracies can result. The problem has previously been treated satisfactorily only for the oversimplified case of monochromatic waves. In the general case, various prescriptions for imposing "spongy" boundary conditions are used -- it is hoped that the progress reported in Report No. 30 will be useful in the solution of this vexing problem in atmospheric dynamics. Second, the lateral boundaries can also reflect internal waves in a stratified fluid giving spurious results. Again, the appropriate radiation boundary condition should be applied. In summary, it is exceedingly important for numerical simulations of stratified flows to make use of the proper boundary conditions, otherwise improper effects of the stratification, like downstream as well as upstream blocking, may result. With the boundary conditions of the type discussed in Report No. 30, these difficulties are expected to disappear.

TASK II

PART A

CALCULATION OF STABLY STRATIFIED FLOW
AROUND COMPLEX TERRAIN

BY

DOUGLAS K. LILLY

Calculation of Stably Stratified Flow
Around Complex Terrain

by

Douglas K. Lilly

Flow Research, Inc., Kent, Washington 98031

The purpose of this note is to derive and demonstrate a method for calculating the flow around and through complex terrain when thermal stratification is sufficiently strong that a part of the flow cannot pass over the terrain. It is suggested that this method might be useful for determining the transport of pollutants introduced into the atmosphere above the boundary layer but well below the tops of terrain obstacles. The application may be somewhat more general if a turbulent boundary layer model is incorporated into the lower part and a simplified wave model can be fitted to the top. From a more fundamental point of view the results show how the difficulties associated with blocking of flow across two-dimensional obstacles essentially disappear when a more realistic three-dimensional terrain is introduced.

It is known that when the kinetic energy of a stably stratified fluid stream impinging upon an obstacle is smaller than the potential energy required to lift it over the obstacle, the flow will be blocked to some degree upstream of the obstacle. The basis of the present method is the assumption that each layer of the blocked flow resembles two-dimensional (horizontal) potential flow around the contours of the terrain at that level, and that the deviations from two-dimensional potential flow can be deduced as higher order terms in a convergent series expanded about a small parameter.

In the following we develop the formal series solution and illustrate its application by means of an analytic solution for a simple terrain shape. More realistic solutions would require numerical methods and also should take account of the separation of the quasi-potential flow from the back side of the mountain as well as boundary friction and heat transport effects.

The steady state incompressible inviscid Boussinesq equations of motion, continuity, and conservation of buoyancy may be written in dimensionless form as

$$\frac{\partial}{\partial x} \left(\frac{u^2 + v^2}{2} + p \right) - v\zeta + w \frac{\partial u}{\partial z} = 0 \quad (1)$$

$$\frac{\partial}{\partial y} \left(\frac{u^2 + v^2}{2} + p \right) - u\zeta + w \frac{\partial v}{\partial z} = 0 \quad (2)$$

$$\left(\frac{h^2}{L^2} \right) \left(u \frac{\partial w}{\partial x} + v \frac{\partial w}{\partial y} + w \frac{\partial w}{\partial z} \right) + \frac{\partial p}{\partial z} + \rho = 0 \quad (3)$$

$$\frac{\partial u}{\partial x} + \frac{\partial v}{\partial y} + \frac{\partial w}{\partial z} = 0 \quad (4)$$

$$\frac{U^2}{h^2 N^2} \left(u \frac{\partial \rho}{\partial x} + v \frac{\partial \rho}{\partial y} + w \frac{\partial \rho}{\partial z} \right) - w = 0 \quad (5)$$

The variables have been scaled as follows. Horizontal coordinates x and y by L , a characteristic horizontal mountain dimension; vertical coordinate z by h , the mountain height; horizontal velocities u and v by U , a characteristic horizontal velocity below the mountain top level; vertical velocity w by hU/L ; disturbance pressure $p - \bar{p}(z)$ by $\rho_0 U^2$; disturbance density $\rho - \bar{\rho}(z)$ by $U^2 \rho_0 / gh$, where ρ_0 is a reference density. The pressure and density scaling were chosen so that the pressure disturbance would be of the same nominal magnitude as the horizontal kinetic energy fluctuations, and the density scaling so that the hydrostatic terms in (3) would be of the same nominal magnitude.

The above scaling introduces two dimensionless parameters. The first, in Eqn. (3), is simply the ratio of the height to the width of the mountain, and if that is small it suggests use of the hydrostatic equation, which we assume to be appropriate. The second parameter, in Eqn. (5), is an internal Froude number of inverse gross Richardson number, where $N^2 = -\frac{g}{\rho_0} \frac{\partial \bar{\rho}}{\partial z}$. This Froude number is essentially the ratio of the

mean flow kinetic energy to the potential energy required to lift fluid over the mountain from the ground. In cases of significant blocking the parameter is small. Equation (5) suggests an expansion solution in powers of the Froude number, with the lowest order solution a purely horizontal flow. Thus we assume the expansion as follows:

$$\begin{aligned}
 u &= u^{(1)} + \epsilon u^{(2)} + \epsilon^2 u^{(3)} + \dots \\
 v &= v^{(1)} + \epsilon v^{(2)} + \dots \\
 w &= \epsilon w^{(2)} + \dots \\
 p &= p^{(1)} + \epsilon p^{(2)} + \dots \\
 \rho &= \rho^{(1)} + \epsilon \rho^{(2)} + \dots
 \end{aligned} \tag{6}$$

where $\epsilon = U^2/h^2 N^2$.

Upon substitution of the above expansion into Eqns. (1) - (5) we obtain the first order equations as

$$\frac{\partial}{\partial x} \left(\frac{u^{(1)2} + v^{(1)2}}{2} + p^{(1)} \right) = v^{(1)} \zeta^{(1)} \tag{7}$$

$$\frac{\partial}{\partial y} \left(\frac{u^{(1)2} + v^{(1)2}}{2} + p^{(1)} \right) = -u^{(1)} \zeta^{(1)} \tag{8}$$

$$\frac{\partial p^{(1)}}{\partial z} + \rho^{(1)} = 0 \tag{9}$$

$$\frac{\partial u^{(1)}}{\partial x} + \frac{\partial v^{(1)}}{\partial y} = 0 \tag{10}$$

If we multiply (7) by $u^{(1)}$, (8) by $v^{(1)}$ and add, it is seen that the Bernoulli equation is satisfied along a streamline of the first order velocity. Also by differentiating (7) with respect to y and (8) with respect to x and subtracting, we can obtain a similar equation for conservation of first order vorticity. Since the two-dimensional continuity equation, (10), allows the formation of a stream function $\psi^{(1)}$, these relations may be specified as

$$\frac{u^{(1)2} + v^{(1)2}}{2} + p^{(1)} = \text{function}(\psi^{(1)}) \quad (11)$$

$$\text{and} \quad \zeta^{(1)} = \nabla^2 \psi^{(1)} = \text{function}(\psi^{(1)}) \quad (12)$$

If an upstream velocity distribution were specified it would be possible to solve (12) for the flow, (11) for the pressure, and (9) for the density. In a simpler case, however, we simply assume that the incoming free stream flow is irrotational, so that the solution required is that of potential flow around the mountain contour at each z -level independently. Note that the free stream velocity may be an arbitrary function of height, and not dimensionless unity as implied by the scaling of Eqns. (1) - (5). Note also that the addition of the Coriolis parameter to the vorticity in Eqns. (7), (8), and (12) need not cause any significant change unless the horizontal scales are so large that the variation of the Coriolis parameter with latitude must be considered.

The most important second order equation is that arising from substituting definitions (6) into (5), the buoyancy conservation equation. This leads to the relation

$$w^{(2)} = u^{(1)} \frac{\partial \rho^{(1)}}{\partial x} + v^{(1)} \frac{\partial \rho^{(1)}}{\partial y} \quad (13)$$

From this, the divergent part of the second order horizontal velocity may be obtained from integration of the continuity equation and the rotational part and the second order pressure from the second order contributions to (1) and (2).

To show results of this solution from an analytically solvable case we choose a constant free stream velocity equal to unity and a mountain with circular contours, i.e.,

$$x^2 + y^2 = F(x) \text{ at the mountain surface} \quad (14)$$

Then the irrotational flow solution around such a mountain will be given by the derivatives of the velocity potential $\phi^{(1)}$, which may be obtained conventionally by assuming a source sink pair at the origin $x=y=z=0$. The potential function and the velocities are given by

$$\phi^{(1)} = \cos\theta (r + F/r) \quad (15)$$

$$v_r^{(1)} = \frac{\partial \phi^{(1)}}{\partial r} = \cos\theta (1 - F/r^2) \quad (16)$$

$$v_\theta^{(1)} = \frac{1}{r} \frac{\partial \phi^{(1)}}{\partial \theta} = -\sin\theta (1 + F/r^2) \quad (17)$$

where r is the distance from the origin and θ the angle in cylindrical coordinates. From Eqns. (11) (with the function equal to $1/2$, that is half the free stream velocity squared), we then obtain $p^{(1)}$, and from (9) and (13) $\rho^{(1)}$ and $w^{(2)}$ as follows:

$$p^{(1)} = \frac{F}{r^2} (\cos 2\theta - F/2r^2) \quad (18)$$

$$\rho^{(1)} = -\frac{F'}{r^2} (\cos 2\theta - F/r^2) \quad (19)$$

$$w^{(2)} = \frac{2F'}{r^3} (\cos 3\theta - \frac{3F}{r^2} \cos\theta + \frac{2F^2}{r^4} \cos\theta) \quad (20)$$

The higher order terms for the divergent and rotational velocities become considerably more difficult to compute, analytically at least.

At the mountain surface $F = r^2$. From this we can see the general trend of the solution. Eqn. (17) shows that the first order flow vanishes at the normal stagnation point and is twice the mean stream velocity at the edge. The pressure is high at the stagnation point and low at the edge, as expected. The disturbance density, and therefore the vertical displacement, vanishes at the stagnation point (but not upstream of it) and is negative at the edge (if $F' < 0$, corresponding to a mountain width decreasing with height). The vertical velocity also vanishes

at the stagnation point and at the edge, but is first upward then downward upstream of the stagnation point and downward in the acceleration region.

It is not obvious whether a zone of convergence can be readily established for this solution. An idea of the probable zone of convergence can be obtained by looking at the conditions under which the first order stratification, $\partial \rho^{(1)} / \partial z$, is of the same magnitude as the mean stratification. At such a location the first order streamlines may cross and the solution becomes unrealistic. This can be shown to occur when $|\partial \rho^{(1)} / \partial z| = \epsilon^{-1}$, i.e. when $\epsilon = r^2 / (F''(\cos 2\theta - F/r^2) - F'^2/r^2)$. It always occurs first at the mountain surface, $F = r^2$, but the details depend on the precise form of F chosen.

For an ellipsoidal (spherical in the scaled coordinates) mountain, $r^2 + z^2 = 1$. If $\epsilon = 0.1$ the probable zone of convergence is below $z = 0.51$. For $\epsilon = 0.2$ it is below $z = 0.27$, and no convergence can apparently be obtained if $\epsilon > 0.25$. On the other hand for a conical mountain, $r^2 + z = 1$, the limiting condition is simply $\epsilon = (1-z)^2$, so that there is a probable zone of convergence for all values of $\epsilon < \text{unity}$. The meaning of the non-convergence at higher levels is not completely clear but it must be associated with the fact that a complete solution of any mountain wave problem requires an upper boundary condition. The apparent convergence of the above solution close to the ground implies that the solution there is independent of the upper boundary condition. It may be speculated that the upper part of the present solution could be used as a boundary condition for a linearized lee wave solution in the upper regions but there may be an intermediate region where neither approximation is sufficiently valid.

TASK II

PART B

NUMERICAL SIMULATION OF RADIATION BOUNDARY
CONDITIONS BY DAMPING

BY

M. ISRAELI

STEVEN A. ORSZAG

Table of Contents

	<u>Page</u>
Table of Contents	i
1. Introduction	B-1
2. Steady Oscillations	B-6
3. Initial - Value Problems	B-11
4. Reference	B-12
5. Figure	B-13

Flow Research Report No. 30

Numerical Simulation of Radiation Boundary
Conditions by Damping

by

M. Israeli and Steven A. Orszag
Flow Research, Inc., Kent, Washington 980311. Introduction

Radiation boundary conditions appear in a wide variety of physical problems involving wave propagation. With mixed initial-boundary value problems of hyperbolic partial differential equations, boundary conditions should be specified for dynamical quantities propagating on characteristics entering the domain of integration, while no boundary conditions are necessary for quantities propagating on characteristics leaving the domain. If the domain of integration is finite, numerical solution of such a problem may be effected by standard techniques, such as the finite-difference method. On the other hand, if the desired region of integration is infinite, numerical solution encounters difficulty because of the necessary limitation of the computational domain to a finite region. With initial-value or radiation problems, the appropriate boundary conditions at infinity are normally "radiation boundary conditions"; that is, the amplitude of waves entering from infinity are required to be zero, while no conditions are placed on outgoing waves propagating to infinity. With scattering problems, the amplitude of an incoming wave from infinity is specified and the amplitudes of the "scattered" outgoing waves emanating from the physical domain are sought; scattering problems can be easily reformulated as radiation problems. The difficulty with numerical solution of these problems is transferring the desired boundary condition at infinity to a condition at the finite boundary of the computational domain. Many important problems await proper resolution of the above difficulty, including flow past a body or obstacle in a stratified fluid.

The mathematical difficulty is best brought out by the simple problem of the one-dimensional wave equation

$$u_{tt} = u_{xx} \quad (0 \leq x < \infty) \quad (1)$$

with radiation boundary conditions at ∞ ,

$$u(0,t) = f(t) \quad (t > 0)$$

and the special initial conditions

$$\begin{aligned} u(x,0) &= 0 \\ u_t(x,0) &= 0 \end{aligned} \quad (0 < x < \infty)$$

The exact solution to this problem is

$$u(x,t) = \begin{cases} 0 & t < x \\ f(t-x) & t \geq x \end{cases} \quad (2)$$

The difficulty with numerical solution of the problem is that if arbitrary boundary conditions are placed at any finite boundary used to simulate the infinite region then arbitrary and wrong results are gotten. For example, if the boundary condition $u = 0$ is applied at $x = L$, the solution to (1) becomes

$$u(x,t) = \sum_{n=0}^{\infty} [f(t-x-2^n L) - f(t+x-2^{n+1} L)], \quad (3)$$

where $f(t)$ is extended to negative t as $f(t) = 0$ for $t < 0$. The solution (3) is identical to (2) only for $0 \leq t < L$. Beyond $t = L$, waves are 'reflected' off the boundary $x = L$ and there is a finite discrepancy between (3) and (2). When numerical solution proceeds using such boundary conditions at $x = L$, the simulation of (2) can be faithful everywhere only for $t < L$, and near $x = 0$ only for $t < 2L$. For $t > 2L$, the reflected waves reach $x = 0$ and completely change the solution there from the desired outgoing solution. Of course, the numerical solution is useful for $t < L$ so that if L is large enough, the solution remains useful for a long time. However, in practice, L can not be taken very large (especially in two and three dimensional problems) because of limited computer resources so that the solution obtained within the finite domain is completely unsatisfactory.

For the problem (1), a satisfactory solution to the above difficulty would be application of the radiation boundary condition

$$u_t + u_x = 0 \quad \text{at } x = L. \quad (4)$$

With (4), the solution to (1) within $0 \leq x \leq L$ is precisely (2); waves do not reflect from $x = L$ with the boundary condition (4). The problem (1) may be solved satisfactorily using numerical methods with (4) applied at $x = L$. However, this does not solve the general problem of radiation boundary conditions. For example, with the two-dimensional wave equation in polar coordinates,

$$u_{tt} = u_{rr} + \frac{1}{r} u_r + \frac{1}{r^2} u_{\theta\theta}, \quad (5)$$

the generalization of (4) at the finite outer boundary $r = L$ is

$$u_t + u_r = 0 \quad (6)$$

However, with (6) errors of order $1/r$ are made in the radiation condition, so that unless L is very large, the errors due to (6) will limit the accuracy of the numerical solution to (1). Further difficulty with boundary conditions like (4) or (6) is anticipated in more difficult problems where either the linear wave dispersion relation remains intractable or nonlinearities, strong inhomogeneities, etc. are present.

Another method for handling the problem of an infinite domain that may at first seem appropriate is a coordinate transformation of the infinite domain to a finite domain or, nearly equivalently, the use of a nonuniform grid in finite difference approximation to (1). For example, the coordinate transformation

$$z = 1 - \exp(-x) \quad (7)$$

transforms $0 \leq x < \infty$ into $0 \leq z < 1$. Equation (1) becomes

$$u_{tt} = (1-z)^2 u_{zz} - (1-z) u_z. \quad (8)$$

It would seem that numerical solution of (8) on the uniform grid $z_n = n/N$, $n = 0, \dots, N$ would give accurate solution of (1) with the radiation conditions. In effect, this would amount to use of the nonuniform grid

$$x_n = \ln \frac{1}{1-z_n} \quad (9)$$

directly on (1).

Unfortunately, however, this method cannot work in general. It is well known (cf. Orszag and Israeli 1974) that difference approximations to a wave problem require high resolution per wavelength of the solution in order to be accurate; typically, order 10 grid points per wavelength are required for, say 10% accuracy. Thus, if the typical wavelength of the exact solution is λ , we require grid spacing $\Delta x < 1/10 \lambda$ or, from (9),

$$\frac{1}{N} = \Delta z_n < (1 - z_n)^2 \frac{1}{10} \lambda,$$

which is violated when

$$1 - z_n < \sqrt{\frac{10}{N\lambda}}.$$

Thus, the waves cannot be adequately resolved near $z = 1$. What then happens to the resolution depends on the numerical scheme; in general, inadequately resolved waves reflect from the grid. In essence, if the wave between grid point x and $x+h$ is not resolved because the wave oscillates too rapidly then the coupling between the grid points is like that between two weakly coupled mass points one of which is oscillating rapidly. The oscillation in one does not effectively drive an oscillation in the other; for the present problem there is a direct analog to the boundary condition $u = 0$ at $x = L$ or (1), so that reflected waves result.

The trouble with mapped coordinates can be seen already from (8) where $z = 1$ appears as a singularity of the spatial part of the equation. Mapping just sweeps the radiation condition problem under the rug, where it can still befoul numerical solution.

The purpose of this paper is to investigate the application of still another technique for imposing radiation boundary conditions, namely damping. If damping is imposed on all waves propagating near the outer boundaries of the finite computational domain, then the outgoing waves are reduced in amplitude when they hit the outer boundary and reflect, while the reflected waves are reduced in amplitude as they propagate in from the outer boundary to the region near $x = 0$ of most interest. By properly 'tuning' the damping to the problem, it is hoped to minimize the errors from the reflected waves and thus, permit faithful numerical solution of the problem. Of course,

introduction of weak damping is the standard mathematical artifice for analytic solution of steady state wave problems. With any (arbitrarily small) damping, incoming waves from infinity are damped to zero amplitude by the time they reach any finite region of space, while outgoing waves are but slightly damped in any given finite region if the damping is small enough. In the limit of zero damping, the solution satisfying the desired radiation boundary condition is obtained.

2. Steady Oscillations

The most transparent way to impose damping on (1) is to first rewrite it as the system

$$\begin{aligned}v_t &= w_x \\w_t &= v_x\end{aligned}$$

where $v = u_t$, $w = u_x$. With second order (Newtonian viscosity) damping, the system is

$$\begin{aligned}v_t &= w_x + \nu(x)v_{xx} \\w_t &= v_x\end{aligned}\quad (10)$$

We consider the solution of (10) on the interval $0 \leq x \leq L$ with boundary conditions

$$\begin{aligned}w(L,t) &= 0 \\v(0,t) &= \sin kt = \operatorname{Im}(e^{ikt})\end{aligned}\quad (11)$$

If we look for solutions of the form $v = \operatorname{Im}(\hat{v}(x)e^{ikt})$, it follows that

$$\hat{v}_{xx} + \frac{k^2}{1+ik\nu(x)} \hat{v} = 0\quad (12)$$

When $\nu = 0$, the outgoing wave solution is $\hat{v} = e^{-ikx}$.

When ν is constant, there are solutions to (12) of the form $\exp(i\alpha x)$ where

$$\alpha = \pm k/\sqrt{1+ik\nu} = \pm \hat{\alpha}.\quad (13)$$

The boundary conditions (11) are satisfied by the solution

$$\hat{v} = \frac{\cos \hat{\alpha} (L-x)}{\cos \hat{\alpha} L}.$$

The error relative to the exact outgoing wave $\exp(-ikx)$ is

$$\varepsilon(x,t) = \operatorname{Im} [(\hat{v}(x) - e^{-ikx})e^{ikt}]$$

so that the maximum error at any x is

$$\varepsilon_{\max}(x) = \left| \hat{v}(x) - e^{-ikx} \right|$$

Several limiting cases are of interest:

- (i) $\nu k \ll 1$, $\nu k^2 L \ll 1$. In this case $\hat{\alpha} \ll k - \frac{1}{2} i \nu k^2$ so that

$$v(x,t) \sim \sin kt \cos k(L-x)/\cos kL, \quad (15)$$

which is just the same standing wave obtained without damping. In this limit, the effect of damping is everywhere negligible.

- (ii) $\nu k \gg 1$. In this limit, $\hat{\alpha} \sim \frac{1}{2} \sqrt{\frac{k}{\nu}} (1-i)$, so that the wave is distorted. In the limit $k^2 L^2 \gg \nu k$, it follows that

$$\hat{v}(x) \sim \exp\left(\frac{1}{2} \sqrt{\frac{k}{\nu}} (i-1)x\right) \quad (16)$$

- (iii) $\nu k \ll 1$, $\nu k^2 L \gg 1$. In this limit, the maximum error is

$$\varepsilon_{\max}(x) \sim 1 - e^{-\frac{1}{2} \nu k^2 x}, \quad (17)$$

so that accurate simulation of the outgoing wave can be achieved on a fixed interval $0 \leq x \leq x_0$ provided $x_0 \ll L$. In fact, the conditions of case (iii) can be reinterpreted as follows. First, $\nu k \ll 1$ can be rewritten $\nu k^2 \ll k$ so that the requirement is that the damping rate be much smaller than the wave frequency. Second, the condition $\nu k^2 L \gg 1$ requires $kL \gg 1$, so that the number of wavelengths in the computational domain is large. The latter requirement together with the condition $x_0 \ll L$ shows that the constant damping is a very poor way to achieve radiation conditions. In fact, a more careful analysis of the maximum error than provided by (17) would show that there are two essential kinds of error in $\hat{v}(x)$ which may be termed phase error and damping error. Phase error is that error induced in the frequency of the outgoing wave by the presence of the damping, while the damping error is due both to damping of the outgoing wave and the unwanted reflected wave. In the present limit, phase error is negligible.

In order to make error of order ε in the region $0 \leq x \leq x_0$, it is necessary that

$$e^{-\frac{1}{2}\nu k^2 x_0} \sim 1 - \varepsilon, \quad (18)$$

while
$$e^{-\nu k^2 L} \sim \varepsilon \quad (19)$$

In other words, we require

$$\frac{x_0}{L} \sim \frac{2\varepsilon}{\ln \frac{1}{\varepsilon}}, \quad \nu k^2 x_0 \sim 2\varepsilon$$

With $\varepsilon = .01$, $k = x_0 = 1$, it follows that we must choose $L \sim 250$, $\nu \sim .02$. Thus, 99.6% of the computational domain is "wasted", hardly a satisfactory situation.

The above analysis can be extended to other damping factors. With various $\nu(x)$, (12) can be solved analytically in terms of special functions like Airy functions, hypergeometric functions, etc. However, the most general results are obtained by WKB analysis. The WKB solution to (12) is

$$\hat{v} \sim \left[\frac{1-ik\nu(x)}{1-ik\nu(0)} \right]^{\frac{1}{4}} \frac{\cos \left[k \int_x^{I'} \frac{ds}{\sqrt{1-ik\nu(s)}} \right]}{\cos \left[k \int_0^L \frac{ds}{\sqrt{1-ik\nu(s)}} \right]} \quad (20)$$

Error less than ε for $0 \leq x \leq x_0$ requires

$$\begin{aligned} k^2 \int_0^{x_0} \nu(x) dx &\lesssim 2\varepsilon \\ k^2 \int_0^L \nu(x) dx &\gtrsim \ln \frac{1}{\varepsilon} \end{aligned} \quad (21)$$

which are the generalizations of (18), and (19).

For example, if we wish to choose the optimal damping factor with $\nu(x) = \nu x^n$ for given ratio of useful to total computational domain, x_0/L ,

then we must satisfy

$$\frac{1}{n+1} v k^2 x_o^{n+1} \sim 2\varepsilon$$

$$\frac{1}{n+1} v k^2 L^{n+1} \sim \ln \frac{1}{\varepsilon}$$

so that

$$\left(\frac{x_o}{L}\right)^{n+1} \sim \frac{2\varepsilon}{\ln \frac{1}{\varepsilon}} \quad (22)$$

In other words, as n increases, the maximum error on $0 \leq x \leq x_o$ decreases (at least while the above approximations are valid). For example, with $x_o = \frac{1}{3}L$ and $n = 4$ then $\varepsilon \sim .01$. With $x_o = k = 1$, it follows that $v \sim .06$, $L \sim 3$.

The condition for applicability of the WKB approximation is

$$\frac{d\lambda}{dx} \ll 1, \quad \lambda = \frac{2\pi}{k} \sqrt{1 - ikv(x)},$$

or with $v(x) = vx^n$, $nvx^{n-1} \ll 1$. If we require this condition everywhere, then we must have

$$nv L^{n-1} \ll 1. \quad (23)$$

This condition is not satisfied by the above example. However, the weaker condition $nvx_o^{n-1} \ll 1$ for validity of WKB on $0 \leq x \leq x_o$ is satisfied. It may be shown by lengthy and complicated turning point analysis of the WKB solution that this weakened condition is sufficient for the present application.

We have studied the solution to (12) numerically. Rewriting (12) as

$$\hat{v}_{xx} + \alpha^2(x)\hat{v} = 0, \quad (24)$$

we used the fourth-order difference approximation

$$(A(x+h)+1)\hat{v}(x+h) + (10A(x)-2)\hat{v}(x) + (A(x-h)+1)\hat{v}(x-h) = 0 \quad (25)$$

where $A(x) = [\alpha(x)]^2 h^2 / 12$. The boundary conditions on (25) are $\partial v / \partial x = 0$ at $x = L$, $v(0) = 1$, the former being applied with $O(h^3)$ accuracy by Taylor expansion.

The calculations were performed with various k and $v(x)$ on the interval $0 \leq x \leq \pi$ (i.e., $L = \pi$). The results for the maximum error $\epsilon_{\max}(x)$ are shown in Fig. 1. For example, a maximum error of 4% on the interval $0 \leq x \leq x_0 = \frac{1}{3}\pi$ is achieved by $v(x) = .05x^4$ when $k = 3$. Among all coefficients in $v(x) = vx^4$, $v = .05$ gives the smallest maximum error. For $k = 6$, the error can be reduced to 2% with $v = .004x^4$ over the same interval. Again the coefficient $v = .004$ is optimal. According to (22), $x_0 = \frac{1}{3}L$ should give 1% errors when $n = 4$.

For larger values of x_0/L , the errors are larger. With $v(x) = .04x^2$, the error is 21% for $x_0/L = \frac{1}{2}$. (The latter example was chosen at random with no effort given to optimization).

The present calculations are meant to be just an illustration of how best choices for $v(x)$ can be made. More detailed analyses will be presented later.

3. Initial-Value Problems

The above analysis on the effect of damping in steady-state problems can be misleading for time-dependent computations because of slowly decaying transient effects.

Consider the case of $v(x) \equiv v$ so that

$$u_{tt} = u_{xx} + vu_{xxt} \quad (26)$$

with initial conditions

$$\begin{aligned} u(x,0) &= 0 \\ u_t(x,0) &= 0 \end{aligned}$$

and boundary conditions

$$\begin{aligned} u(L,t) &= 0 \\ u(0,t) &= \sin kt . \end{aligned}$$

This problem may be solved easily by Laplace transform in t giving the Laplace transform

$$U(x,p) = \frac{k}{p^2+k^2} \frac{\sinh p(L-x)/\sqrt{1+pv}}{\sinh pL/\sqrt{1+pv}} \quad (27)$$

The poles of $U(x,p)$ at $p = \pm ik$ give the persistent part of the solution as $t \rightarrow \infty$, namely (14). However, $U(x,p)$ has other poles at

$$\frac{pL}{\sqrt{1+pv}} = in\pi \quad (n \neq 0) \quad (28)$$

i.e.,

$$p = -(\nu n^2 \pi^2 \pm \sqrt{\nu n^4 \pi^4 - 4L^2 n^2 \pi^2})/2L^2$$

$$\approx -\frac{\nu n^2 \pi^2}{2L^2} \pm in\pi ,$$

the latter holding when $\nu n^2 \pi^2 \ll 4L^2$. The decay rates of these transient modes are $\nu n^2 \pi^2 / 2L^2$. In particular, if $L = \pi$, the most persistent transient persists for the time $2/\nu$, which may be very long. In fact, this effect gives much larger errors in time-dependent problems than may be expected on the basis of the steady state analysis in Section 2. We have made

several different kinds of numerical experiment to verify this behavior. Indeed, we found much larger errors than could be explained on the basis of the steady state analysis.

In ~~summary~~ summary, our analysis indicates the drawbacks and pitfalls encountered in imposition of radiation boundary conditions. To date, we believe that the best approach is to use appropriate boundary conditions like (4) and (6) on radiation boundaries, together with optimized damping, as explained in Section 2.

Reference:

Orszag, S. A., and Israeli, M. 1974. Ann. Rev. Fluid Mech. 6, xxx.

Figure Captions:

Fig. 1 Spatial dependence of the error with damping factor $\nu(x)$.

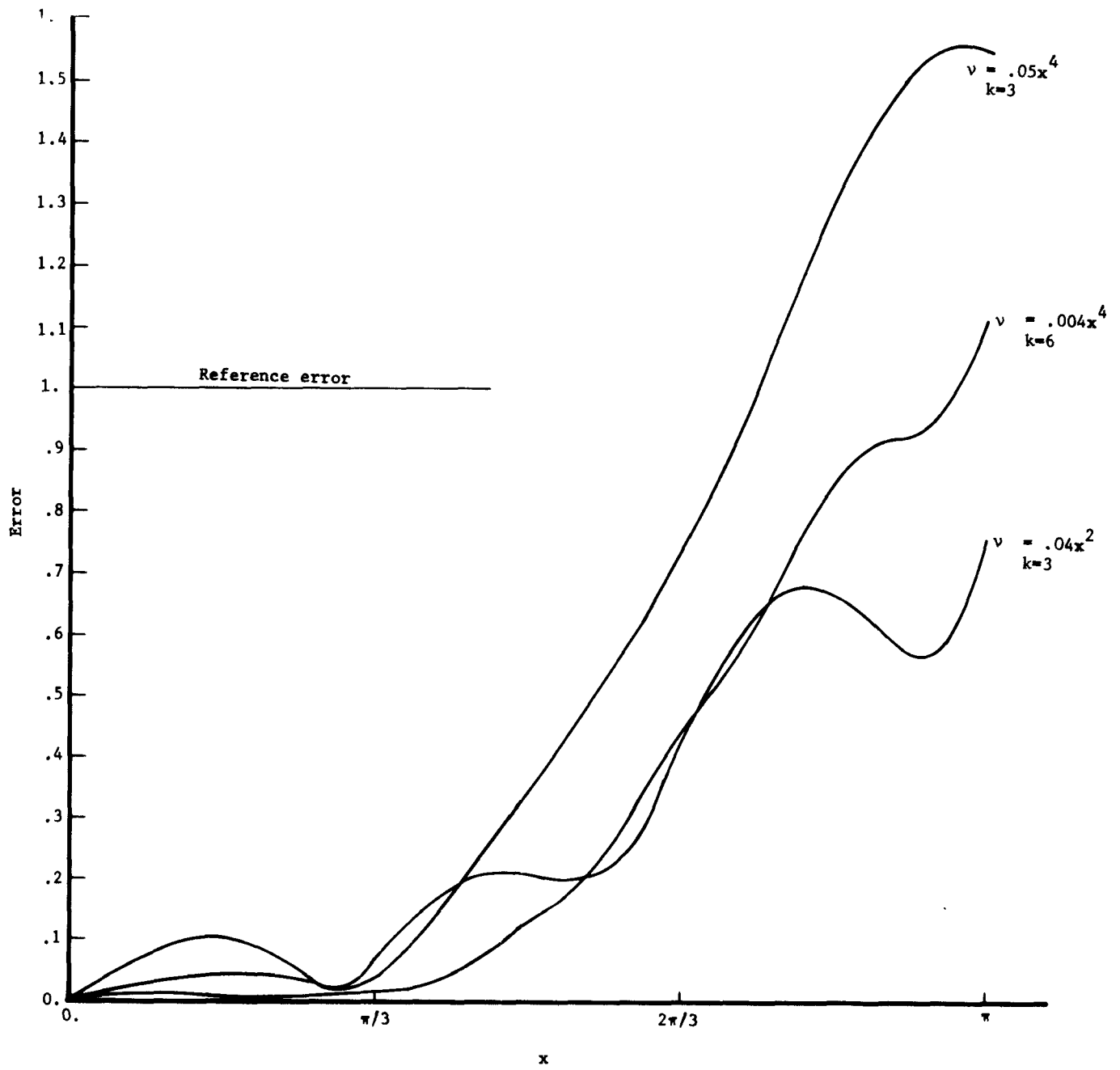


Fig. 1 Spatial dependence of the error with damping factor $v(x)$

ENVIRONMENTAL PROTECTION AGENCY
Technical Publications Branch
Office of Administration
Research Triangle Park, N.C. 27711

OFFICIAL BUSINESS

AN EQUAL OPPORTUNITY EMPLOYER

POSTAGE AND FEES PAID
ENVIRONMENTAL PROTECTION AGENCY
EPA - 335



Return this sheet if you do NOT wish to receive this material ☐,
or if change of address is needed ☐. (Indicate change, including
ZIP code.)

PUBLICATION NO. EPA-650/4-74-044